ACS APPLIED NANO MATERIALS

www.acsanm.org Article

Laser-Ablative Engineering of ZrN-Based Nanoparticles for Photothermal Therapy and SERS-Based Biological Imaging

Andrei I. Pastukhov, Victoria O. Shipunova, Julia S. Babkova, Ivan V. Zelepukin, Micah Raab, Rebecca Schmitt, Ahmed Al-Kattan, Artem Pliss, Andrey Kuzmin, Anton A. Popov, Sergey M. Klimentov, Paras N. Prasad,* Sergey M. Deyev,* and Andrei V. Kabashin*

Cite This: https://doi.org/10.1021/acsanm.4c01970 Read Online

ACCESS | Metrics & More | Article Recommendations | Supporting Information

ABSTRACT: Zirconium nitride (ZrN) nanoparticles (NPs) can offer appealing plasmonic properties for biomedical applications, but the synthesis of nontoxic, water-dispersible nanoformulations exhibiting plasmonic features in the biotransparency window presents a great challenge. Here, we report the synthesis, by methods of laser ablation, of small ZrN-based NPs, which are unique in combining photothermal heating and near-field enhancement in the transparency window. Depending on the synthesis environment, the formed ZrN-based NPs exhibit plasmonic absorption bands with maxima around 660−670 and 610−630 nm, which are largely red-shifted compared to what is expected from pure ZrN NPs. The observed shift is explained by the inclusion of zirconium oxide ZrO_x ($1 < x < 2$) into NP composition and NP coating by naturally formed ZrO_x. We then explored biophotonic applications of ZrN NPs. While pure NPs demonstrate their nontoxicity in vitro, their conjugation with anti-HER1 affibody $Z_{HER1:1907}$ and subsequent photothermal heating with NIR-I laser cause 100% cancer cell death. In addition, profiting from the field enhancement, we demonstrate bioimaging functionality using a designed surface-enhanced Raman scattering probe based on an NP-conjugated azobenzene-CN-OH molecule as a Raman reporter. Combining a strong photothermal effect and the imaging option, laser-synthesized ZrN/ZrO_x NPs promise a major advancement of theranostic modalities based on plasmonic nanomaterials.

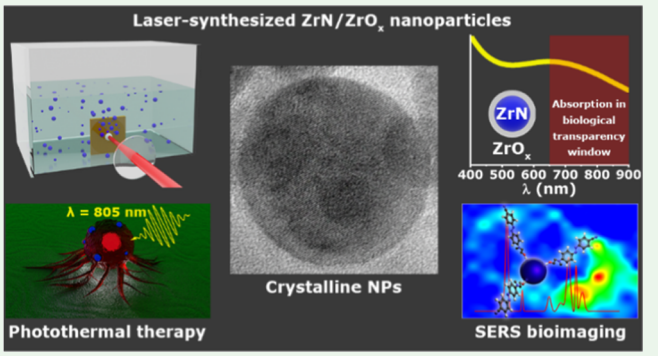

KEYWORDS: *pulsed laser ablation in liquids, plasmonic nanomaterials, ZrN nanoparticles, photothermal therapy, SERS, bioimaging, biomedical applications*

INTRODUCTION

Plasmonic nanomaterials are now in the focus of interest in biomedical research as promising contrast agents in bioimaging and sensitizers of therapies.[1−3] These materials are unique in supporting free-electron oscillations, termed surface plasmons, under optical excitation, which leads to a resonant absorption/scattering of light in a particular spectral range and a variety of related phenomena.[4] Since the efficiency of plasmonic absorption can exceed that of organic dyes by 3−4 orders of magnitude,[4] they can serve as extremely efficient sensitizers of photothermal therapy (PTT) to eliminate cancer cells via a local overheating (hyperthermia),[5−7] as well as contrast agents in photoacoustic bioimaging.[8] On the other hand, the excitation of plasmon resonances is often accompanied by a strong enhancement of near-field, which can be used to enable the surface-enhanced Raman scattering (SERS) channel, known as a "fingerprint" of molecules, to detect and identify trace amounts of molecules[9,10] or design Raman tags for bioimaging and bioidentification.[11]

The photothermal and near-field enhancement capabilities of plasmonic nanomaterials depend on optical constants and excitation dynamics and can substantially vary for different materials and compositions. Owing to their chemical stability, good biological compatibility, and distinct plasmonic properties, gold (Au) nanostructures have been considered the main plasmonic material for biomedical applications. As shown in Figure 1, owing to particular optical constants together with ultrafast local relaxation, Au nanoparticles (NPs) combine a high absorption cross-section (σ_{abs}) coupled with efficient thermal relaxation to yield efficient phototherapy applications, as well as high near-field enhancement $|E_{max}/E_0|$, enabling

Received: April 7, 2024
Revised: July 31, 2024
Accepted: August 1, 2024

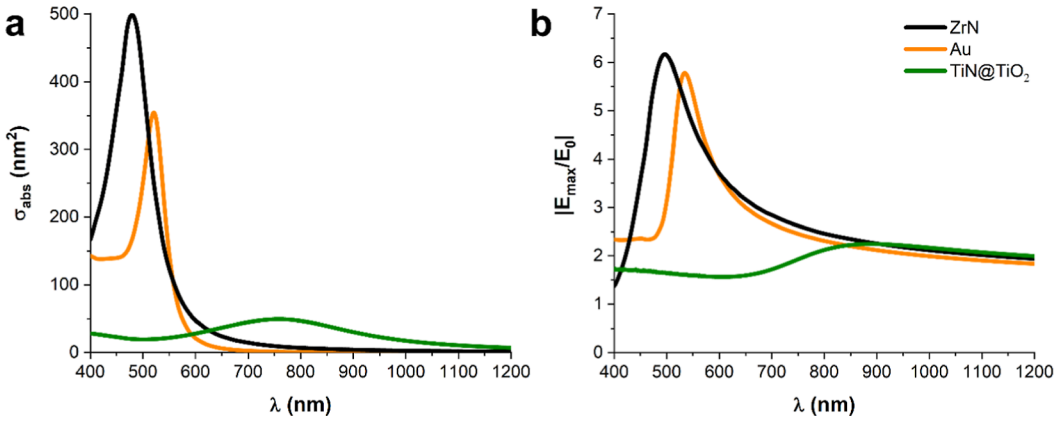

Figure 1. Spectral dependence of calculated absorption σ_{abs} (a) and near-field enhancement $|E_{max}/E_0|$ (b) coefficients for 20 nm Au NPs (orange curves), 20 nm core@shell TiN@TiO_2 NPs (green curves), and 20 nm pure stoichiometric ZrN NPs (black curves) NPs. All calculations were performed by using COMSOL software.

SERS and other near-field-related applications. However, the absorption peak of spherical Au NPs of different sizes ranges between 520 and 560 nm,[4] which is outside the biological transparency window (630−900 nm), complicating the projected phototherapy applications. Therefore, one has to engineer complex structures such as Au-based core−shells,[12,13] nanorods,[14] or nanocages[15] to shift this peak toward this window. Although such engineered structures solve the spectral mismatch problem, their use is not free of problems. As an example, anisotropic structures such as the nanorods often lose their shape and related plasmonic properties during the photothermal procedure,[16,17] while core−shells have a weak conversion of light energy to absorption as most of it goes to scattering.[4] In addition, engineered nanostructures can induce acute toxicity problems due to the use of non-biocompatible chemical agents such as CTAB[18] or delivery in vivo issues due to the very large size of some structures (for example, the size of core−shells often exceeds 120−150 nm[12]).

Nanomaterials based on transition metal nitrides are now actively discussed as alternative plasmonic structures which could provide similar spectral features in absorption/scattering and be used in a variety of applications, including nanophotonics, photovoltaics, and biophotonics.[19−21] Titanium nitride (TiN) NPs have gained most attention among nanomaterials of this class due to their low cost and high availability and the possibility of generation of a red-shifted plasmonic peak compared to gold. When properly architectured, TiN NPs can provide plasmonic features in the biological transparency window (typically, around 670−720 nm; see an example in Figure 1, green curves) with almost all light energy acquired by absorption and then converted to heat,[21] which makes them a very promising system for photoacoustic bioimaging and phototherapy.[22,23] Zirconium nitride (ZrN) NPs are another potentially interesting plasmonic material based on metal nitrides. The optical response of ZrN NPs significantly differs from that of TiN counterparts as ZrN-based nanostructures are capable of providing not only a strong photoabsorption efficiency (Figure 1a) but also an efficient near-field enhancement option (Figure 1b). As illustrated by a black curve in Figure 1a, the plasmonic peak from 20 nm NPs of pure ZrN is in the blue range (450−480 nm), which is outside the biological transparency window. However, some previous studies[24] reported the possibility of shifting the plasmonic peak toward 600 nm and higher due to the inclusion of oxynitrides and coating of the NP surface by a thin ZrO_2 shell. Despite promising plasmonic properties, ZrN NPs have not yet been the focus of biomedical studies due to the difficulty of fabricating ZrN-based nanostructures of appropriate geometry and composition, which could combine the generation of plasmon features in the biological transparency window with low toxicity and easy water dispersibility in the absence of aggregation and precipitation effects. Indeed, chemical synthesis pathways for the synthesis of transition metal nitrides typically employ hazardous products such as hydrochloric acid,[25] making them hardly useful for biological use, while dry techniques such as plasma synthesis[24] or electric discharge-based wire explosion[26] normally provide aggregated structures which are hardly dispersed in liquids and then tend to precipitate.

Based on a natural production of nanoclusters during laser action on a solid target, followed by their coalescence to form NPs, laser ablation presents a viable alternative to conventional chemical and dry synthesis pathways,[27−29] which could be adapted for the fabrication of ZrN-based nanostructures. The first attempt at the synthesis of ZrN-based NPs was undertaken using laser ablation in a gaseous environment. Reinholdt et al.[30] adapted a technique of laser ablation/evaporation from a zirconium nitride powder target, followed by adiabatic expansion of ablation products in a residual N_2 gas, to form NPs composed of an almost stochiometric crystalline ZrN core, coated by a thin shell of zirconium oxides and oxynitrides.[30] The authors recorded a certain red shift of extinction spectra compared to pure ZrN NPs (around 530−560 nm), which was probably related to a particular shell composition. Although the authors did not study the dispersion of these NPs in liquids, we can imagine similar problems as those for NPs prepared by dry methods. We believe that the task of engineering proper architectures of ZrN-based nanostructures for biomedical applications can be solved by using methods such as pulsed laser ablation in liquids (PLAL), in which the NPs are formed directly in the liquid.[28,31,32] As we showed in previous papers,[32,33] PLAL in the ultrashort (femtosecond) pulse regime makes possible fine-tuning of the size and structural characteristics of formed NPs, while the oxidation state and geometry of nanomaterials can be controlled by adjusting radiation parameters and the environment (oxygen-saturated or oxygen-free water, ethanol, and acetone).[34,35] Here, we explore the use of femtosecond laser

https://doi.org/10.1021/acsanm.4c01970
ACS Appl. Nano Mater. XXXX, XXX, XXX−XXX

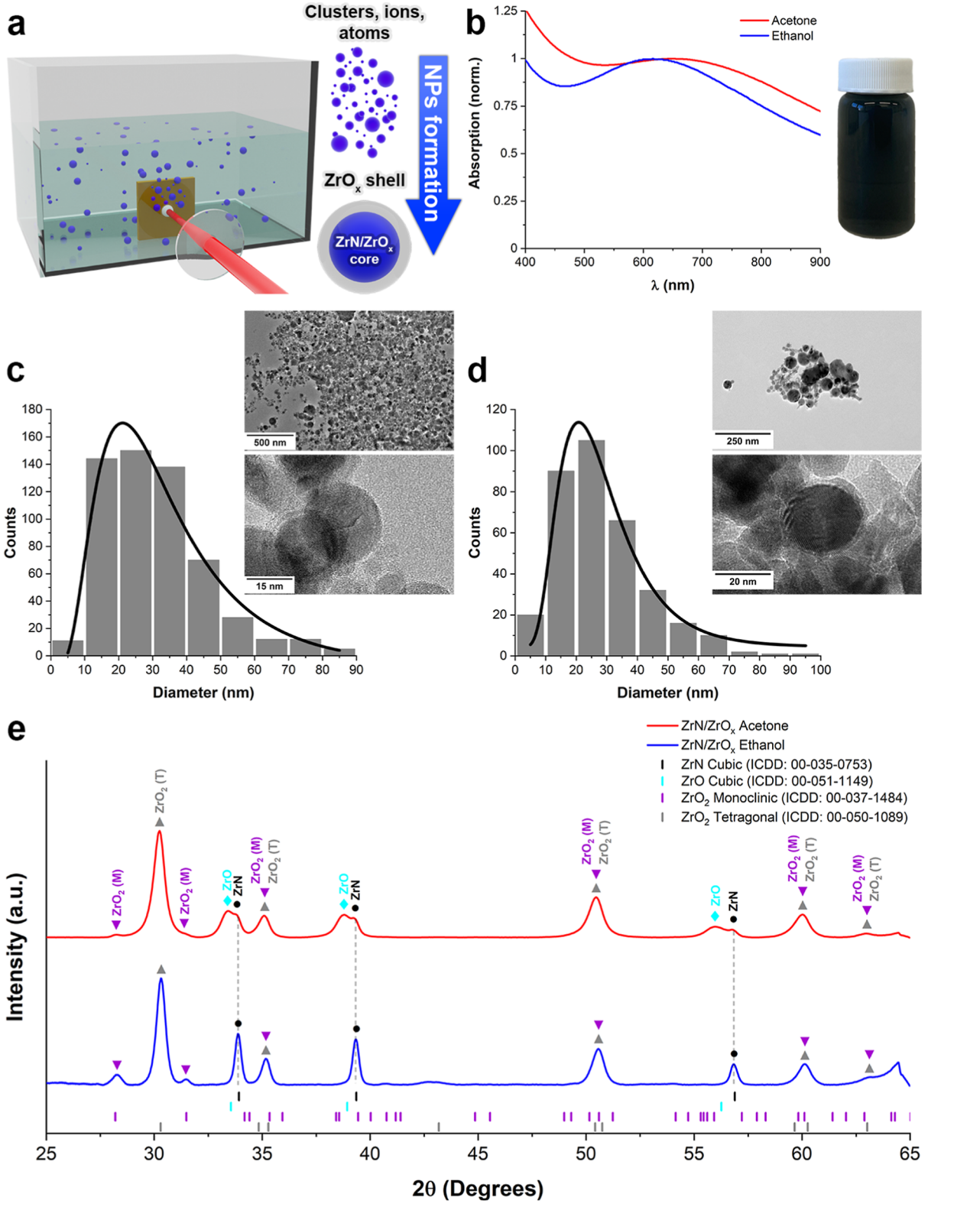

Figure 2. Laser-ablative synthesis and properties of ZrN-based NPs. (a) Schematics of laser-ablative synthesis. A focused beam from a Yb:KGW femtosecond laser irradiates a ZrN target placed in a glass cuvette filled with acetone or ethanol. The laser ablation process leads to the production of ZrN-based NPs and their release into the surrounding solvent; (b) optical absorption spectra from laser-synthesized ZrN-based NPs prepared in acetone (red) and ethanol (blue). The inset demonstrates a photo of a typical solution of prepared ZrN NPs; (c,d) typical TEM images (upper insets) and corresponding size distribution of NPs prepared by laser ablation in acetone (c) and ethanol (d). The lower insets in panels (c,d) show high-resolution images of several NPs; (e) XRD patterns from NPs prepared by laser ablation in acetone (red pattern) and ethanol (blue pattern). Table positions of crystalline ZrN and different zirconium oxide states (ZrN cubic, ZrO cubic, ZrO_2 monoclinic, and ZrO_2 tetragonal) are indicated below the patterns.

https://doi.org/10.1021/acsanm.4c01970
ACS Appl. Nano Mater. XXXX, XXX, XXX−XXX

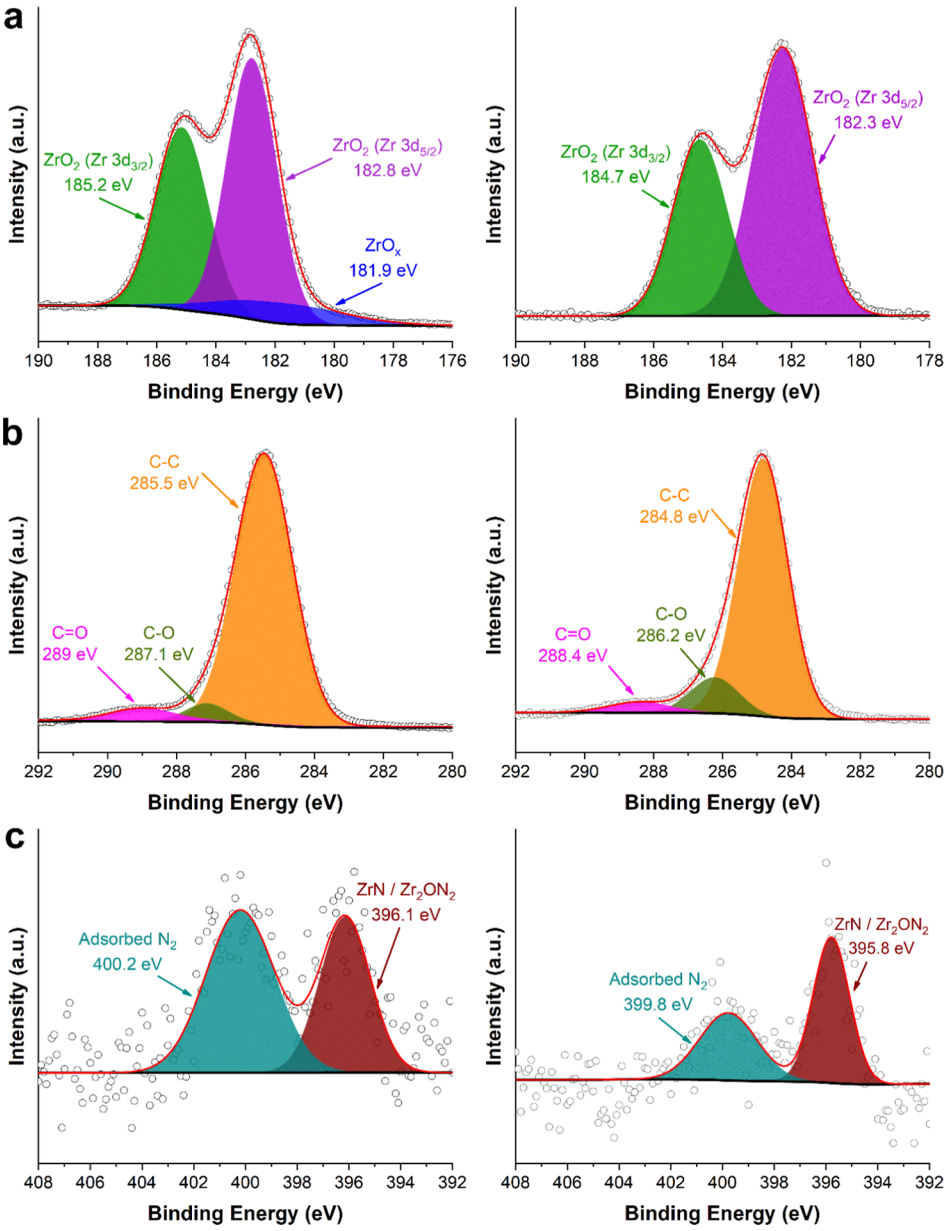

Figure 3. High-resolution XPS measurements for samples prepared in acetone (left) and ethanol (right). (a) Zr 3d; (b) C 1s; (c) N 1s core levels.

ablation in organic solutions (acetone and ethanol) to synthesize ZrN-based nanomaterials for biophotonic applications. We show that such a method can lead to the fabrication of ZrN-based NPs, which exhibit distinct plasmonic resonances in the region of relative biological transparency with maxima depending on the used environment (660−670 and 610−630 nm for acetone and ethanol solvents, respectively). We then show that the formed ZrN-based NPs have a very low toxic profile and demonstrate a strong therapeutic effect on EGFR-overexpressing cells under 805 nm light illumination. Finally, profiting from near-field enhancement ability, we show the possibility of designing SERS probes for bioimaging based on chemical assembly of ZrN-based NPs and azobenzene Azo-CN-OH molecule as a Raman reporter. Combining photothermal and near-field enhancement abilities, the laser-synthesized NPs promise the development of novel theranostic modalities based on plasmonic nanomaterials.

RESULTS

Laser-Ablative Synthesis and Physicochemical Characterization of ZrN-Based NPs. In our experiments, a beam from a fs laser (Yb:KGW, 1030 nm, 490 fs) was focused on a ZrN target, which was fixed in a vertical position in a quartz cuvette filled with 50 mL of acetone or ethanol and constantly moved to minimize the ablation from the same target area (Figure 2a, see detailed description in the Materials and Methods section). We observed a dark-blue coloration of the solution just after the beginning of the ablation process, which evidenced the formation of ZrN-based NPs. The NP solution reached a concentration of 150 μg mL^{-1} after 45 min of the ablation process, and the formed solutions were very stable, with no sign of precipitation for several months of storage at ambient conditions. As shown in Figure 2b, ZrN-based NPs prepared in acetone and ethanol exhibited broad plasmonic absorption bands with peak maxima around 660−670 and 620 nm, respectively, which are highly red-shifted compared to

https://doi.org/10.1021/acsanm.4c01970
ACS Appl. Nano Mater. XXXX, XXX, XXX−XXX

what is expected from pure stoichiometric ZrN NPs (Figure 1a). In both cases, the absorption spectra had a long tail in the near-infrared (over 800 nm), promising attractive applications in photothermal therapy. As shown in Figure S1 (Supporting Information), absorption largely dominates the extinction spectra of ZrN NPs compared to scattering. It should be noted that the NPs could be transferred from organic solutions to an aqueous environment with negligible changes in absorption spectra and without any size change or loss of colloidal stability (Figure S2).

To unravel the structural properties of ZrN-based NPs and clarify the origin of the observed red-shifted positions of absorption peaks, we examined them by different methods. Figure 2 shows typical transmission electron microscopy (TEM) images and corresponding size distributions of ZrN-based NPs prepared by femtosecond laser ablation in acetone (c) and ethanol (d). One can see that in both cases, the average (mode) size of the formed NPs was about 21 nm, which is close to optimal size values for biomedical applications. A detailed analysis of NP morphology by high-resolution TEM (HR-TEM) revealed their core−shell geometry (see an example in the lower inset of Figure 2c,d), which can be explained by the formation of zirconium oxide states during the oxidation of the NP surface. According to HR-TEM images shown in Figure S3a−e, the core and shell regions possess crystalline structures for both samples prepared in acetone and ethanol. In particular, for the sample prepared in acetone, we detected the presence of tetragonal ZrO_2 in the shell structure [2.96 Å, (101) plane, Figure S3a], whereas the core was composed of ZrN [2.68 Å, (111) plane, Figure S3b]. It is worth noting that for samples prepared in ethanol, oxide phases were present in the cores of NPs (Figure S3c−e). Importantly, apart from ZrO_2 in the tetragonal phase [2.94 Å, (101) plane, Figure S3c], we identified crystalline phases related to zirconium suboxides Zr_3O [3.44 Å, (101) plane, and 4.85 Å, (100) plane, Figure S3d,e].[36]

To clarify the composition and crystalline state of the formed ZrN-based NPs, we performed X-ray diffraction (XRD) analysis of the NP powder. XRD patterns of ZrN-based NPs prepared in acetone and ethanol are shown in Figure 2e by red and blue colors, respectively. One can see that a ZrN cubic phase is present in both samples, which is confirmed by the appearance of several relevant peaks (ICDD: 00-035-0753). Our analysis also reveals the presence of crystalline phases of monoclinic and tetragonal (ICDD: 00-037-1484 and 00-050-1089) ZrO_2 (m-ZrO_2 and t-ZrO_2, respectively), which may indicate a partial oxidation of the formed NPs, most probably due to the formation of a thin oxide shell, in accordance with the HR-TEM image presented in the lower inset of Figure 2c. Unexpectedly, we also detected a signal corresponding to zirconium monoxide ZrO (ICDD: 00-051-1149) from the NPs prepared in acetone, which was absent in the case of NPs synthesized in ethanol. To the best of our knowledge, the ZrO structure is unstable.[37] Therefore, we can conclude that the ZrO state could be included in the ZrN matrix as a result of nonequilibrium nanocluster growth, which is one of the trademarks of the PLAL technique.[27,28] We can also suppose that the presence of zirconium oxide states in the NP composition could be responsible for a drastic red shift of observed absorption spectra compared to what is expected from pure ZrN (Figure 1, black spectra), while a more red-shifted position of the absorption peak from NPs prepared in acetone (Figure 2b) can be explained by the presence of an additional zirconium oxide state (ZrO) in NPs prepared in acetone. In general, our experiments evidenced that the formed ZrN-based NPs present a mixture of ZrN and ZrO_x ($1 < x < 2$) and can be denoted as ZrN/ZrO_x NPs. Using the Scherrer equation, we estimated crystallite sizes of different Zr-related compounds. As shown in Table S1, the calculated average values are in the range of 14−23 nm, which is consistent with TEM data. Such an analysis also evidences that NPs can contain oxide and nitride mixed phases assembled together in a single nanostructure.

To support our assumptions about the core−shell nature of the formed NPs, we examined superficial layer states by X-ray photoelectron spectroscopy (XPS). Results of XPS data analysis are shown in Figure 3a−c. One can see from Figure 3a that for samples prepared both in acetone (left) and ethanol (right), peaks associated with ZrO_2 (Zr $3d_{3/2}$ and Zr $3d_{5/2}$) were detected in the Zr 3d region.[38] It is worth noting that a weak peak of the zirconium suboxide ZrO_x state was recorded for the sample prepared in acetone,[39] which is consistent with results of our measurements using HR-TEM and XRD techniques. Indeed, according to XRD patterns (Figure 2e), zirconium monoxide ZrO was detected only for the sample prepared in acetone, whereas for ethanol-related samples, it was absent. In contrast, our HR-TEM measurements confirmed the presence of crystalline structures composed of the Zr_3O hexagonal phase,[40] although XRD data did not confirm it. We suppose that the formation of such phases is due to a partial decomposition of the metastable ZrO cubic phase and its transformation into stable ZrO_2 and Zr_3O phases.[37] Furthermore, it is known that the formation of monoxide and suboxide phases is unlikely in the superficial layer and is typically detected in the interlayer regions of layered structures. Note that the C 1s region (Figure 3b) contains peaks associated with typical traces of carbon contamination.[41] It is important that zirconium carbide phases, which usually locate at binding energies of about 282 eV,[42] were absent in our measurements. Thorough analysis of peaks in the N 1s region (Figure 3c) evidences a partial absorption of nitrogen from the atmosphere (~400 eV), whereas peaks around 396 eV indicate the presence of zirconium nitride ZrN and zirconium oxynitride Zr_2ON_2 compounds in both samples.[43,44] We believe that the signal associated with Zr_2ON_2 comes from the bottom part of the oxide shell as a transition layer between the core and the shell.

To estimate the atomic concentration of each element, we recorded XPS survey spectra for different types of ZrN-based NPs (Figure S4a,b). Our analysis showed that the concentration of nitrogen was negligible, indicating the absence of nitride-related compounds on the surface of NPs (see Table S2). Indeed, oxygen was the dominant element, which obviously originated from SiO_2 (glass substrate) and ZrO_2 (NP shell) compounds.

Modeling of the Optical Response of ZrN-Based NPs. To further clarify possible reasons for observed red shifts in the plasmonic spectra and investigate their properties, we carried out simulations using COMSOL Multiphysics (RF module, see the Materials and Methods section for detailed information) to calculate absorption cross-section (σ_{abs}) and near-field enhancement $|E_{max}/E_0|$ for different compositions and architectures of ZrN/ZrO_x nanostructures. The diameter of the NPs in our model (21 nm) was selected to correspond to the average (mode) size of NPs synthesized in acetone and ethanol (Figure 2c,d). All calculations were performed for

https://doi.org/10.1021/acsanm.4c01970
ACS Appl. Nano Mater. XXXX, XXX, XXX−XXX

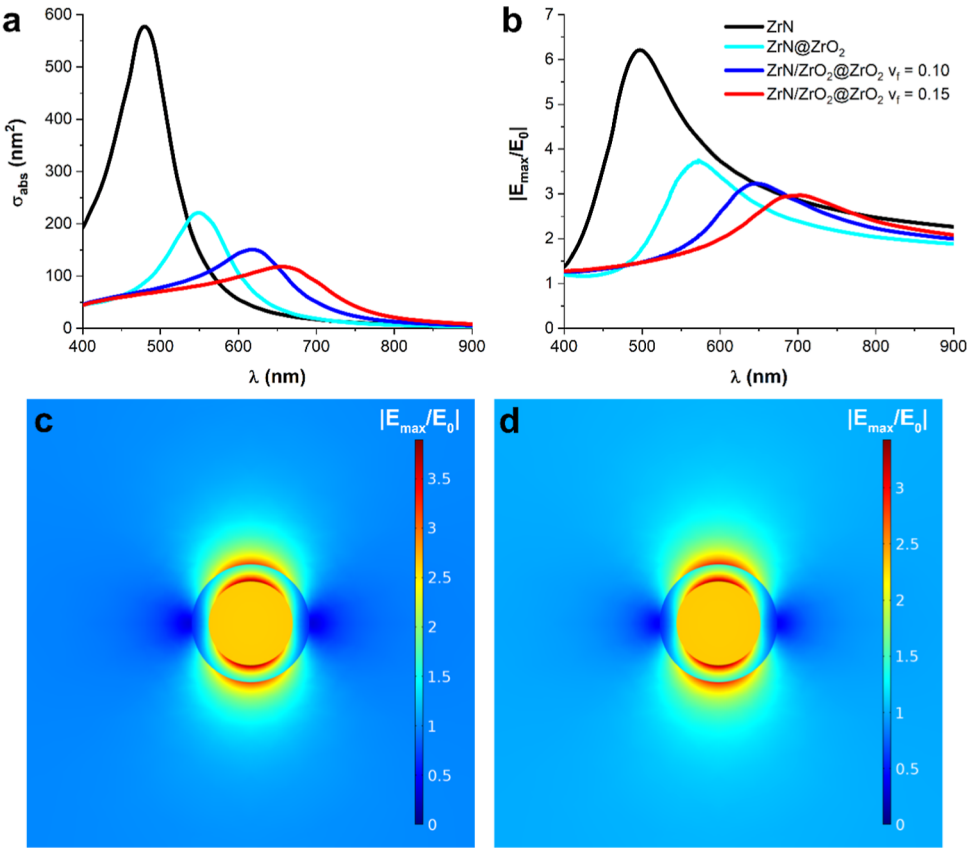

Figure 4. Calculated plasmonic absorption and field enhancement properties of ZrN-based NPs. (a) Absorption cross-section σ_{abs}. Calculations were performed by assuming water as the surrounding medium. (b) Near-field enhancement properties. The spectra are calculated outside the NP shell on the ZrO_2/water interface. Field enhancement distributions ($|E_{max}/E_0|$) for ZrN-based NPs having the volume fraction v_f = 0.1 at λ = 647 nm (c) and for the NPs having v_f = 0.15 at λ = 684 nm (d).

water dispersions. As follows from our experimental data, the shift of plasmon resonance is negligible when NPs are transferred from organic solutions (ethanol and acetone) to water (Figure S2).

A black line in Figure 4a shows a calculated absorption spectrum from pure stoichiometric ZrN NPs as a reference point. It is visible that the plasmonic peak from these NPs is around 470 nm, which does not correspond to our experimental data. We then simulated the situation when the ZrN-based NP core is covered by a 3 nm ZrO_2 shell (without changing the diameter). As shown in Figure 4a by a cyan line, such a coating leads to a shift of position of the absorption peak in accordance with previously published data[24] and a certain (2.5-fold) decrease of the absorption cross-section σ_{abs}, but the shifted value (560 nm) is still not sufficient to explain experimental results. In order to achieve a larger red shift of the peak, we assumed the presence of some oxide states in the NP core, which is indirectly confirmed by the results of our XRD measurements. A model based on the Bruggeman effective medium approximation was applied to calculate the refractive indices of ZrN-based host material containing embedded ZrO_2 clusters inside the core. Calculations were done for different volume fractions (v_f) of ZrO_2 in the ZrN-based core, while the thickness of the oxide shell ZrO_2 was still fixed at 3 nm. As shown in Figure 4a, the addition of ZrO_2 into the NP core can indeed further shift the plasmonic peak, and under v_f = 0.1 and v_f = 0.15, absorption peaks from engineered ZrN-based NPs reach 616 nm (blue line) and 656 nm (red line), which roughly correspond to experimentally measured values for NPs prepared in ethanol and acetone, respectively, to confirm our supposition on the key role of the oxidation phenomena in the red shift of plasmonic spectra. Furthermore, the presence of a higher volume fraction of zirconium oxide in the composition of NPs leads to a larger red shift of the spectrum, which also agrees with the supposition of a higher oxidation state of NPs prepared in acetone, as evidenced by the appearance of additional ZrO lines in the XRD patterns (Figure 2e). It should be noted that the red shifts of the spectra under the addition of oxide states in the core were accompanied by a further decrease of absorption cross-section, but absorption values near resonant maxima at 616 and 565 nm were still very high, exceeding 150 and 110 nm^2, respectively (Figure 4a).

To exclude the scenario in which the position of the absorption peak is determined exclusively due to an alteration of the core composition, we carried out additional calculations. According to our numerical simulations, the increase in oxide content from v_f = 0 up to 0.3 in the ZrN core results only in a slight peak shift of absorption cross-section (Figure S5a, left). Therefore, it is very unlikely that NPs could be composed of a nitride/oxide-mixed core. Another issue is related to the possible formation of a thin carbon layer shell during the fabrication due to the partial decomposition of organic liquids. To check it, we modeled the optical response from a designed artificial nanostructure composed of a ZrN/ZrO_2 core and an amorphous carbon (a-C) shell. Our numerical simulations confirmed a significant shift of the adsorption cross-section peak to the NIR region (Figure S5b, left). However, according to our experimental HR-TEM, XRD, and XPS data, the shell

https://doi.org/10.1021/acsanm.4c01970
ACS Appl. Nano Mater. XXXX, XXX, XXX−XXX

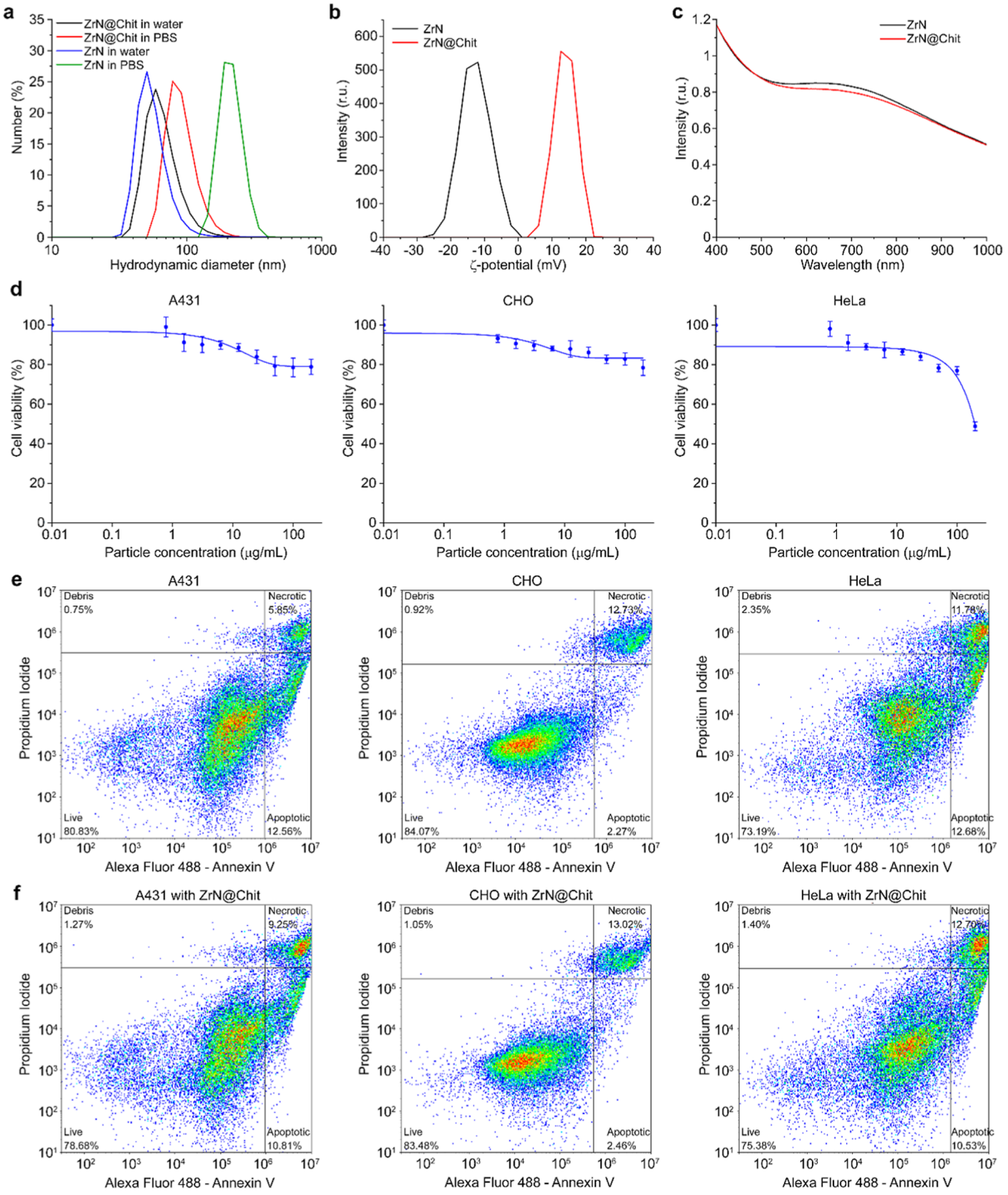

Figure 5. Chitosan coating and cytotoxicity of ZrN-based NPs. (a) Hydrodynamic size distributions of uncoated ZrN NPs and chitosan-coated ZrN@Chit NPs, measured in water and PBS. (b) ζ potential of ZrN NPs and ZrN@Chit NPs. (c) Optical exciton spectra of ZrN NPs and ZrN@Chit NPs. (d) Cytotoxicity of ZrN@Chit particles, measured for A431 (left), CHO (center), and HeLa (right) cell lines. (e,f) Cytometry investigation of the quantity of apoptotic and necrotic cells before (e) and after (f) incubation with ZrN@Chit NPs for A431 (left), CHO (center), and HeLa (right) cell lines.

does not contain carbon and is composed uniquely of different crystalline phases of ZrO_2. Moreover, for the ZrN/ZrO_2@a-C structure with low oxide contents (ν_f = 0 and 0.05), the absorption cross-section peak position is already located near 600 nm, which contradicts our experimentally observed results.

Our calculations also showed that all geometries and compositions of ZrN-based NPs demonstrate a strong near-field enhancement, which looks as an appealing extra option. As shown in Figure 4b, the enhancement efficiency is maximal for pure ZrN and decreases under the red shift of the spectra due to the implantation of oxide states in the form of the oxide shell and further addition of ZrO_2 into the NP core. Despite such a decrease, the efficiency remains remarkable even for the relatively high oxidation state of NPs, as shown by the blue and red lines for ν_f = 0.1 and ν_f = 0.15, respectively. It should be noted that the spectral positions of maximal field enhancement

https://doi.org/10.1021/acsanm.4c01970
ACS Appl. Nano Mater. XXXX, XXX, XXX−XXX

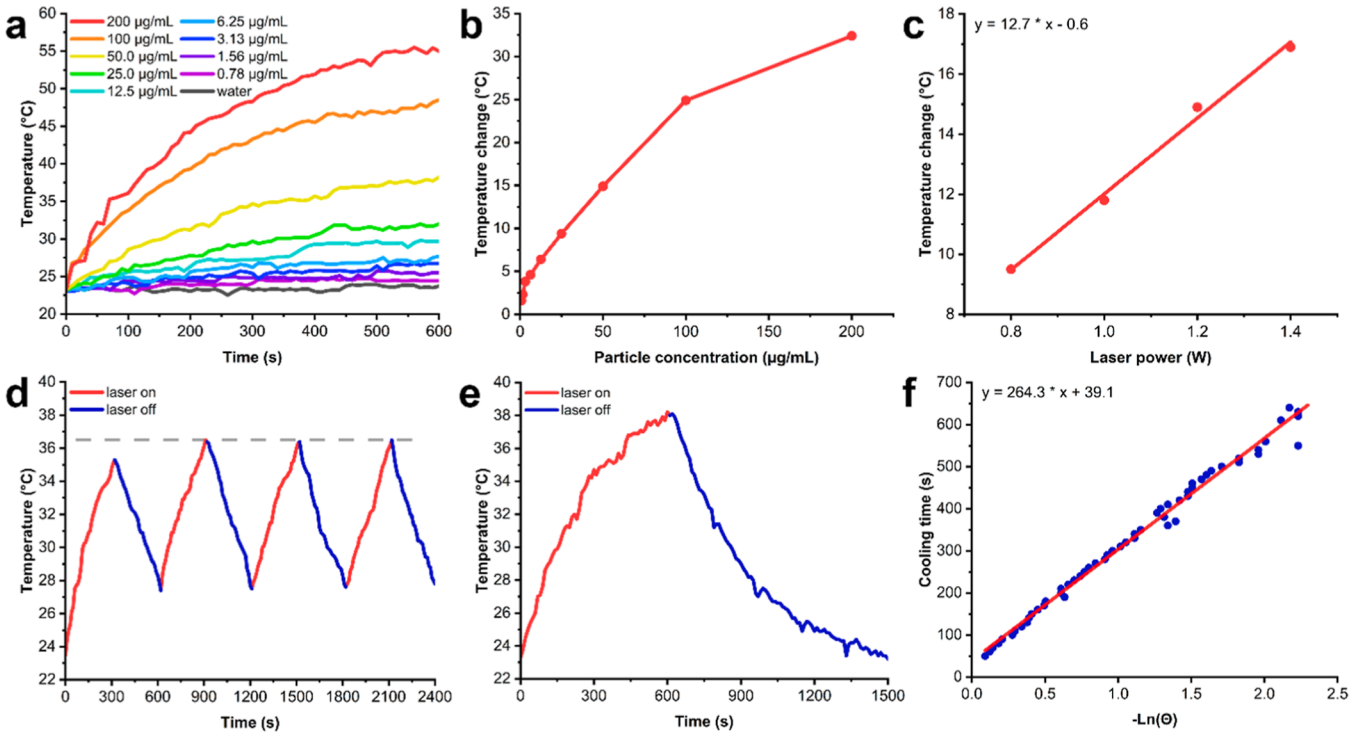

Figure 6. Photothermal properties of ZrN@Chit NPs. (a) Photothermal heating curves of ZrN@Chit aqueous solutions under NIR irradiation at 1.2 W laser power. (b) Dependence of the maximal temperature change on particle concentration under NIR irradiation. (c) Dependence of the temperature change on the laser power. (d) Recycling photothermal stability test with 5 min heating and 5 min cooling steps. (e) Kinetics of the temperature changes during heating for 10 min under NIR irradiation and subsequent cooling. (f) Dependence of cooling time on the negative natural logarithm of the driving force. A solution with a 50 μg mL^{-1} ZrN@Chit particle concentration was used for studies (c–f).

for different NP geometries are slightly red-shifted compared to the maxima of plasmonic absorption. As an example, maximal field enhancements for v_f = 0.1 and v_f = 0.15 are recorded at 647 and 684 nm, respectively, which are 30 nm red-shifted compared to the absorption peaks. Figure 4c,d demonstrates near-field distribution near 21 nm oxide shell-coated ZrN-based NPs with v_f = 0.1 and v_f = 0.15 at wavelengths corresponding to maximal near-field enhancement for these NPs. One can see that similar to plasmonic counterparts (e.g., Au and Ag NPs), the main enhancement takes place on the NP surface, while the presence of the oxide shell does not dramatically decrease the enhancement efficiency. The field enhancement from less oxidized NPs with v_f = 0.1 appears to be higher, suggesting that the NPs prepared in ethanol can have a higher near-field enhancement ability. In general, our calculations confirm the possibility for SERS and other near-field applications of ZrN-based NPs, which look as very attractive options in addition to photothermal capability.

It should be noted that ZrN/ZrO$_x$ nanostructures prepared by laser ablation possess unique properties that are difficult to simulate due to the absence of relevant optical constants in the literature. Therefore, we had to make a set of assumptions. As an example, to model the electrophysical properties of the ZrN/ZrO$_2$ mixed core, we used the Bruggeman effective medium approximation, which obviously does not take into account all interactions within the system. In addition, optical constants for unstable phases such as ZrO (zirconium monoxide) could not be taken into account in the final model because they are not available in the literature. Finally, the theoretically calculated absorption and near-field enhancement properties of ZrN-based NPs can significantly vary depending on the choice of optical constants.[21,24] Therefore, the presented calculation results give a very rough approximation, which qualitatively explains the red shifts of peaks and may not pretend to be a quantitative description of absorption and near-field enhancement efficiencies.

Chemical Modification of ZrN/ZrO$_x$ NPs. To make the NPs functional for biological use, they should be transferred to the biological environment and stabilized to prevent their aggregation. Our tests showed that bare synthesized ZrN-based NPs aggregate in a phosphate buffered saline (PBS) buffer, which mimics physiological conditions. Figure 5a shows that the hydrodynamic size of the NPs increased from 57 ± 18 nm (mode ± half-width of the peak) to 214 ± 42 nm in the buffer. This process was irreversible and took place within the first 15 min of NP incubation, while the final NP size reached 667 ± 144 nm (Figure S6). To achieve prolonged colloidal stability of ZrN-based NPs, they were stabilized via a chitosan oligosaccharide lactate coating. Chitosan oligosaccharide is a biodegradable derivative of a nontoxic cationic carbohydrate polymer having excellent water solubility. The NP coating with chitosan oligosaccharide opens up avenues for their subsequent functionalization by other molecules of interest using the amino and hydroxyl groups presented in the polymer.[45]

Coating efficiency was confirmed by three facts. First, after the coverage, we observed a change in the ζ-potential of NPs (Figure 5b) from originally negative (−12.7 ± 4.4 mV) to a positive one (+13.8 ± 3.2 mV). The positive charge of NPs confirms the presence of protonated terminal amino groups in the chitosan polymer, oriented outward. Second, the hydrodynamic size of the ZrN-based NPs increased from 57 ± 18 nm to 67 ± 22 nm in water due to the attachment of polymer chains on the surface (Figure 5a). Third, the colloidal stability

https://doi.org/10.1021/acsanm.4c01970
ACS Appl. Nano Mater. XXXX, XXX, XXX−XXX

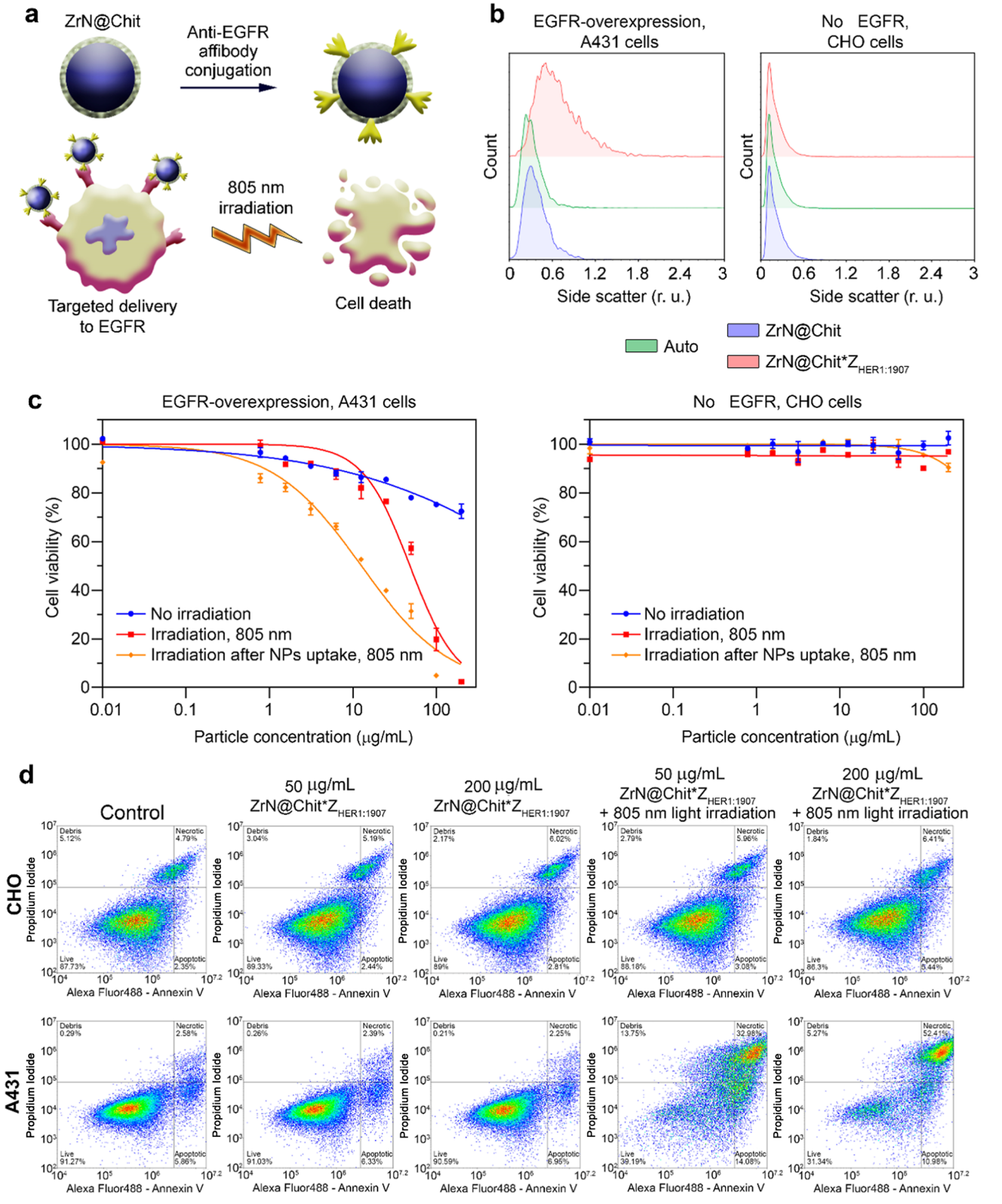

Figure 7. Targeted delivery of ZrN@Chit NPs to EGFR-overexpressing cancer cells and IR-induced cancer cells' death. (a) Scheme of ZrN@Chit NPs labeling with the anti-HER1 affibody, $Z_{HER1:1907}$. (b) Flow cytometry assay demonstrating the high specificity of the ZrN@Chit*$Z_{HER1:1907}$ NP interaction with EGFR-overexpressing A431 cells and the absence of interaction with EGFR-negative CHO cells. Green histograms indicate cells' autofluorescence, blue—cells labeled with ZrN@Chit NPs, and red—cells labeled with ZrN@Chit*$Z_{HER1:1907}$ NPs. (c) MTT assay results showing highly specific toxicity of ZrN@Chit*$Z_{HER1:1907}$ NPs for A431 cells after 5 min of irradiation with an 805 nm laser. Blue lines—without irradiation, red lines—with 805 nm irradiation after 20 min coincubation with NPs, and orange lines—with 805 nm irradiation after 2 h of NP coincubation at 37 °C to ensure their internalization into cells. (d) Cytometry investigation of quantity of apoptotic and necrotic cells before and after incubation with ZrN@Chit*$Z_{HER1:1907}$ NPs and 805 nm laser irradiation for CHO (top) and A431 (bottom) cell lines.

https://doi.org/10.1021/acsanm.4c01970
ACS Appl. Nano Mater. XXXX, XXX, XXX−XXX

of NPs in both PBS and serum greatly increased (Figure 5a). In PBS, we observed a small increase in the hydrodynamic size of chitosan-coated NPs (such NPs will be later labeled as ZrN@Chit) from 67 to 92 nm (Figure 5a), while no change in colloidal stability with time was observed in the presence of serum proteins (Figure S6). Finally, the investigation of optical extinction properties showed that the chitosan coating had a small influence on the plasmonic band (Figure 5c), leading to a slight (~4%) decrease in absorption in the 520−900 nm range, which could be attributed to the increase of NP scattering, but did not provide any significant shift in the peak position.

Photothermal Properties of ZrN@Chit NPs. The high absorption of ZrN@Chit NPs in the near-infrared region makes them attractive for use as sensitizers for photothermal therapy. To study the photothermal properties of ZrN@Chit NPs, we irradiated NP aqueous solutions of various concentrations of 0.78−200 μg mL^{-1} with an 808 nm laser at 1.2 W power and monitored the temperature change of the solutions (Figure 6a). It was shown that at a concentration of 200 μg mL^{-1}, the ZrN@Chit solution temperature increased by 32.4 °C within 10 min of irradiation (Figure 6b), and a solution with a concentration of 25 μg mL^{-1} was heated by 9.4 °C, which is in the optimal range to induce mild hyperthermia.[46] A linear dependence of the change in solution temperature on laser power was observed with a slope of 12.7 °C/W (Figure 6c). The NPs demonstrate good photothermal conversion stability, with the heating temperature remaining constant over several on/off irradiation cycles (Figure 6d). The cooling temperature coefficient τ = 264.3 s was calculated from the cooling kinetics of a solution of ZrN@Chit NPs after 10 min of irradiation (Figure 6e,f). The calculated photothermal conversion efficiency was η = 34.1%, which is comparable to other near-infrared photothermal materials.[47] Therefore, ZrN@Chit NPs have a high light absorption capacity and excellent and stable light-to-heat conversion efficiency, which are essential qualities for PTT agents.

Analysis of ZrN@Chit NP's Cytotoxicity. To evaluate the safety of ZrN-based NPs, we performed two cytotoxicity tests in vitro. First, the MTT analysis was carried out, which assesses cell metabolic activity due to the reduction of colored dye with NAD(P)H-dependent cellular oxidoreductases. Second, flow cytometric analysis using propidium iodide (PI)-stained DNA and Alexa Fluor 488-stained annexin V was performed for the measurement of the ratio of living, necrotic, and apoptotic cells in a population. Three cell lines from different tissues were used for the analysis: human epidermoid carcinoma A431, human adenocarcinoma HeLa, and Chinese hamster ovarian CHO cells. Cells were incubated with 0.78−200 μg mL^{-1} ZrN@Chit NP solutions for 48 h prior to the measurement of cytotoxicity.

Figure 5d shows that NPs had low cytotoxicity according to the MTT test. For all 3 cell lines, the viability was higher than 90, 86, and 77% for concentrations of 1, 10, and 100 μg mL^{-1}, respectively. HeLa cells had a higher sensitivity to ZrN@Chit NPs at a high concentration of nanoagents of 200 μg mL^{-1}, but these cytotoxicity values were comparable with data for other metal nitrides, which are considered safe nanomaterials for biomedical applications. As an example, for the same cell lines, laser-synthesized TiN NPs showed only 65% cell viability at a concentration of 100 μg mL^{-1}.[48] On the other hand, plasmonic gold nanorods at similar concentrations caused severe cell damage of A549 cells due to ROS generation and cell membrane disruption.[49]

To determine if cell viability is altered due to increased cell apoptosis, we treated the same three cell lines: A431, CHO, and HeLa with ZrN@Chit NPs and examined cell apoptosis by flow cytometry. During early apoptosis, phosphatidylserine moves from the inner leaflet of the plasma membrane to the outer leaflet and can bind highly specifically to the green fluorophore-conjugated annexin V protein. During late apoptosis and necrotic cell death, the membranes of dead and damaged cells are permeable to red PI, which binds to DNA. After staining the cell population with Annexin V Alexa Fluor 488 and PI, apoptotic cells with an intact membrane fluoresce green, late apoptotic and necrotic cells show red and green fluorescence, and living cells show little or no fluorescence. To perform positive control with apoptotic and necrotic cells, we measured cells treated with 1 μM staurosporine for 4 h and heated at 75 °C for 10 min, respectively (Figure S7).

Flow cytometric analysis showed that incubation of cells with ZrN@Chit NPs at a concentration of 50 μg mL^{-1} for 48 h does not lead to any significant decrease in the number of living cells. The percentages of live cells untreated and treated with the NPs were 80.83 ± 1.32% and 78.68 ± 0.05% for A431 cells, 84.07 ± 3.04% and 83.48 ± 3.18% for CHO cells, and 73.19 ± 5.49% and 75.38 ± 2.61% for HeLa cells (see representative cytometry images in Figure 5e,f). So, ZrN@Chit NPs demonstrated excellent biocompatibility even in high doses up to 50 μg mL^{-1} in a solution, which opens horizons for the application of this new plasmonic nanomaterial in biomedicine.

Targeted Delivery of ZrN@Chit Particles with the $Z_{HER1:1907}$ Affibody. Specific NP targeting can improve their accumulation in desired cancer cells and decrease nonspecific toxicity. Here, we conjugated ZrN@Chit NPs with a $Z_{HER1:1907}$ affibody, recognizing the EGFR or HER1 receptor with the binding affinity K_d = 43.6 ± 8.4 nM.[50] Since chitosan oligosaccharide lactate contains free amines, ZrN@Chit NPs could be modified with proteins by carbodiimide chemistry via the formation of amide bonds between the carboxyl groups of the affibody and ZrN@Chit amino groups (Figure 7a). A431 cells, which are known to overexpress the EGFR receptor (about 10^7 receptors per cell), were used as a model of cancer cells for the targeted delivery assays, whereas CHO cells, which do not express any ErBB receptor, were used as a control cell line. Flow cytometry confirmed that the FITC-modified $Z_{HER1:1907}$ affibody specifically labels EGFR-overexpressing A431 cells (Figure S8). We also found that EGFR-negative CHO cells do not bind affibodies and can be used as a control cell line.

The specificity of EGFR-targeted ZrN@Chit*$Z_{HER1:1907}$ NPs was evaluated by the flow cytometry method 20 min after particle incubation with the cells. Unique properties of ZrN-based NPs made possible the quantification of cell-binding efficiency via the measurement of changes in cell population side scattering that arise from NPs binding to the cell surface. It is important that such a procedure does not require fluorescent labeling, which always affects NP properties.[51,52] Flow cytometry analysis revealed a significant change in the A431 cell population side scattering only after cell labeling with specifically targeted NPs, without any influence on the control CHO cell line. As shown in Figure 7b, the control ZrN@Chit NPs without targeting modality did not exhibit detectable binding to both A431 and CHO cells. Flow cytometry studies demonstrated 119-fold specificity of the used NPs (for A431,

https://doi.org/10.1021/acsanm.4c01970
ACS Appl. Nano Mater. XXXX, XXX, XXX−XXX

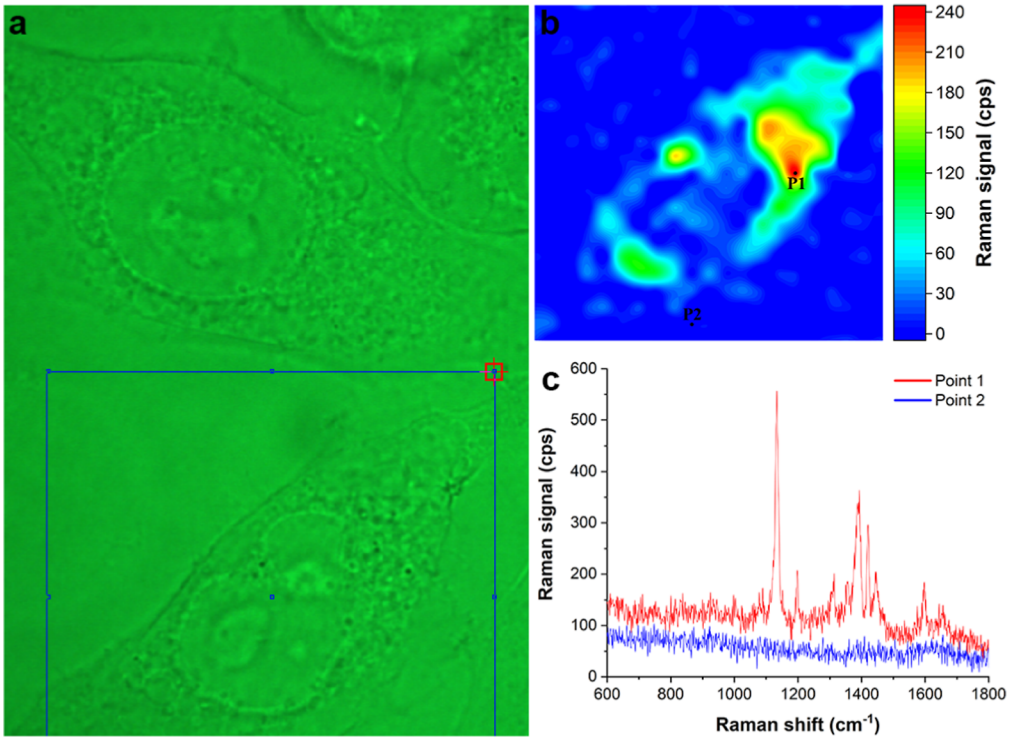

Figure 8. Mapping the distribution of the ZrN@Azo-CN-OH SERS probe by the 1133 cm^{-1}peak of Azo-CN-OH. The laser power is 5 mW@785 nm. (a) Imaged cell in transmission mode; the scanned area is outlined by a blue rectangle. (b) Raman map of the Azo-CN-OH distribution in the imaged cell after 5 h of incubation with NP-conjugation solution. (c) Raman spectrum in cell area pointed out by dots.

ΔSSC = 504,386; ΔSSC = 4231 for CHO cells), which is higher compared to what was previously reported for classical plasmonic nanomaterials.[53] The uptake of targeted NPs to the HER1-overexpressed cancer cell line was additionally quantified by inductively coupled mass spectrometry. ZrN@Chit*$Z_{HER1:1907}$ NPs were incubated for 20 min at 100−400 $\mu g\ mL^{-1}$ concentrations with 10^6 A431 cells mL^{-1}. The uptake of NPs was 3.3 ± 0.9, 8.1 ± 1.2, and 20.7 ± 3.3 $\mu g\ mL^{-1}$ for 100, 200, and 400 $\mu g\ mL^{-1}$ NP concentrations, respectively. So, the binding efficiency was 3.3−5.2% of the added dose of NPs.

IR-Induced Cytotoxicity of ZrN@Chit*$Z_{HER1:1907}$. The ZrN NP-mediated photocytotoxicity was induced by irradiation with an 805 nm laser (1200 mW) for 5 min. Such irradiation leads to NP heating and hyperthermia-induced cell death. On the other hand, this irradiation does not lead to heating of the EGFR-negative cell suspension in the absence of NPs and causes the increase in the temperature of the control cell suspension by only 2.8° at a particle concentration of 50 $\mu g\ mL^{-1}$ and by 7.8° at the maximum used concentration of 200 $\mu g\ mL^{-1}$ (Figure S9). These data suggest that irradiation, even in the presence of NPs, is safe for normal body cells. IR-induced cytotoxicity was evaluated by using a standard MTT assay. Results presented in Figure 7c demonstrate specific IR-sensitized cytotoxicity of ZrN-based NPs only for EGFR-overexpressing A431 cells. As follows from the data analysis, IC_{50} for A431 cells was 2267 $\mu g\ mL^{-1}$ without irradiation and 48.3 $\mu g\ mL^{-1}$ after 5 min irradiation with 805 nm light, which is ca. 50 times less. On the other hand, IC_{50} for CHO cells was not determined since there was no toxic effect on these cells with or without irradiation. Moreover, when cells were incubated with ZrN-based NPs for 2 h at 37 °C to provide their internalization into cells, the IC_{50} value of these particles for A431 cells was reduced up to 12.6 $\mu g\ mL^{-1}$, which is 180 times less in comparison with that of nonirradiated cells.

Then, we measured the number of apoptotic and necrotic cells after incubating ZrN@Chit*$Z_{HER1:1907}$ with A431 and CHO cell lines, as well as following their laser irradiation (Figure 7d). Flow cytometric analysis showed that incubating cells with NPs at concentrations of 50 and 200 $\mu g\ mL^{-1}$ for 48 h did not lead to a decrease in the number of live cells as compared to that of the control group. This confirms that the conjugation of NPs with the $Z_{HER1:1907}$ affibody does not significantly impact their cytotoxicity.

The A431 cell damage significantly increased after NP labeling and 805 nm laser irradiation. After the photothermia for the NP doses of 50 and 200 $\mu g\ mL^{-1}$, we observed the decrease in the quantity of live cells down to 39 and 31%, respectively. The majority of cells were affected by necrotic cell death, which is usual during photothermia. However, the number of apoptotic cell bodies and cell debris also increased (Figure 7d). Importantly, no increase in cell death was observed for the CHO cell line, which confirms the low binding efficiency of ZrN@Chit*$Z_{HER1:1907}$ NPs in these cells.

Then, a clonogenic assay was applied to characterize the cytotoxicity. This test provides more sensitive and reliable results, which depend predominantly on the cell growth mechanisms rather than cell membrane damage, so it is much closer to in vivo cytotoxicity assessment than the MTT assay. The clonogenic assay shows no statistically significant impact of NPs on the CHO cells without expression of the HER1 receptor (Figure S10a,c). At the same time, laser irradiation of A431 cells with ZrN@Chit*$Z_{HER1:1907}$ NPs demonstrated 100% cell death at a 200 $\mu g\ mL^{-1}$ NP concentration (Figure S10a,b). At lower concentrations of NPs of 50 and 100 μg

https://doi.org/10.1021/acsanm.4c01970
ACS Appl. Nano Mater. XXXX, XXX, XXX−XXX

mL^{-1}, laser irradiation decreases the clonogenic ability of cells 1.85- and 4.28-fold, respectively (Figure S10b).

Development of ZrN NP-Based SERS Probes for Bioimaging. The near-field enhancement properties of ZrN-based NPs open up an avenue for their utilization in SERS applications. To design a SERS probe for bioimaging, we employed ZrN-based NPs synthesized in ethanol as they are supposed to exhibit slightly better enhancement properties, according to our calculations (Figure 4b). To develop a Raman marker producing SERS signal enhancement upon excitation in the biologically safe spectral region, we selected an Azo-based Raman reporter based on the Azo-CN-OH molecule (Figure S11a). The nonradiative decay process in Azo produces low fluorescence, which is necessary for sensitive detection of the Raman signal. At the same time, low absorption of this molecule in the NIR region does not produce resonance Raman gain (Figure S11b). A typical signal from the ZrN@Azo-CN-OH conjugate cluster in water deposited on the glass substrate is shown in Figure S12a−c. A number of Azo-CN-OH molecules conjugated to the surface of a single 20 nm ZrN-based NP are estimated to be ∼1000 molecules. A bright spot (Figure S12b) is attributed to a signal from the most intense Azo-CN-OH peak (∼1133 cm^{-1}) and indicates a successful conjugation of the Raman reporter to the NPs surface. Furthermore, the absence of the signal outside the cluster (Figure S12b,c blue region and line, respectively) evidence that the near-field enhancement properties are indeed related exclusively to ZrN-based NPs. However, any quantitative analysis of the conjugate system seems unrealistic since the number of NPs trapped by the laser depends on the experimental conditions. Apart from that, as was mentioned earlier, the field enhancement properties attributed to the agglomerated structure can surpass the theoretically predicted values due to interaction between individual NPs. It is worth noting that the stability of Azo-CN-OH molecules on the NPs surface remained the same as that in the pure state of the compound and was demonstrated in our previous studies.[54]

After incubation of HeLa cells with ZrN@Azo-CN-OH conjugates and subsequent fixation, cells were imaged on a Raman microscope (Figure 8a), and results were mapped using the most prominent Azo-CN-OH peak (∼1133 cm^{-1}). As shown in Figure 8b,c, the signal from the NPs was significantly stronger than the signals from intracellular native components (proteins, lipids, etc.), which allowed us to map the intracellular distribution of NPs with the Raman marker. As expected from vesicle-mediated endocytosis, the Am-CN Azo-OH signal overlapped with the cytoplasmic area and was absent from the cell nucleus (Figure 8a).

DISCUSSION

Nanostructured zirconium nitride presents an alternative plasmonic material to its noble metal counterparts due to a possible combination of photothermal and near-field enhancement abilities. However, the fabrication of ZrN-based nanostructures suitable for biomedical applications is challenging as the formed NP solutions should satisfy stringent biological requirements, including nontoxicity, water dispersibility, and colloidal stability. Chemical synthesis involves complex reactants with strictly defined quasi-equilibrium system parameters as well as toxic byproducts. In the case of ZrN and other transition metal nitrides, the formed NPs are typically contaminated by derivatives of hydrochloric acid and other hazardous products,[25] which are hardly compatible with biological systems. Although dry techniques such as plasma synthesis can be performed under clean conditions to solve the toxic contamination problem, these methods typically lead to relatively aggregated structures that are difficult to disperse and stabilize in aqueous solutions.[24] Another problem is related to the mismatch between the position of the plasmonic feature for pure ZrN NPs (470 nm) and the biological transparency window (Figure 1a). Therefore, the engineering of appropriate complex architectures with included oxide or other states is required to shift the plasmonic feature toward this window.

In this study, we propose an elegant solution to the bottleneck problems in the synthesis of ZrN-based NPs for biomedical applications using the technique of PLAL. Such an approach is free of limitations of chemical methods on the choice of products and, in our case, can be performed under ultrapure conditions (ethanol and acetone) to avoid any toxic contamination, while laser-synthesized NPs are directly released into the liquid medium and electrostatically stabilized to avoid aggregation phenomena. In addition, using the ultrashort laser-ablative regime of PLAL, which is characterized by much lower laser energy required to initiate the process compared to conventional long pulse (ns) ablation,[27] we managed to achieve especially good control of size and structural characteristics of formed nanostructures, similarly to how it was earlier demonstrated for a variety of other nanomaterials, including metal (e.g., Au[32] and B[35] NPs), semiconductor (Si[34] and MoS_2[55]), and composite Fe−Au[56] NPs. Furthermore, profiting from a controlled oxidation environment (ethanol or acetone), we were able to produce ZrN-based nanoarchitectures, which exhibit a red-shifted plasmonic feature compared to pure ZrN NPs with the maxima around 610−630 and 660−670 nm, respectively. As follows from our simulations (Figure 4a,b), such a shift could be due to the presence of implanted ZrO_2 states in the NP core and coating of ZrN-based NPs with an oxide shell. We believe that the implantation of such states becomes possible due to essentially nonequilibrium conditions of nanostructure growth under PLAL. Our data also show that a more red-shifted plasmonic feature from ZrN-based NPs prepared in acetone can be related to a higher volume fraction of zirconium oxide in the composition of NPs, as confirmed by the appearance of additional ZrO lines in XRD patterns of these NPs (Figure 2e). It should be noted that we earlier used the technique of fs laser ablation to fabricate TiN-based NPs, which present a similar group of transition metal nitrides.[23,57] Our tests showed that the oxidation state of these NPs could also be controlled by liquid ambient (water, acetone, ethanol, etc.), while the position of the plasmonic peak also red-shifted from 670 to 720 nm under the increase of the oxidation state.[57]

As was shown, laser-synthesized ZrN-based NPs can be transferred to physiological buffers without any loss of plasmonic properties and stabilized by chitosan coating for further biological use. As follows from our biological assessment, these NPs exhibit very low cytotoxicity for 3 cell lines: A431, CHO, and HeLa cells. As an example, MTT tests evidenced that the viability for all 3 cell lines was higher than 77% for a very high NP concentration of 100 $\mu g\ mL^{-1}$, while flow cytometry tests confirmed excellent biocompatibility even at high doses of 50 $\mu g\ mL^{-1}$ in a solution, which evidence a high safety of ZrN NPs. We believe that the safety of NPs is largely due to the cleanliness of laser-ablative synthesis, which does not involve toxic byproducts. It should be noted that laser-synthesized TiN NPs demonstrated a slightly higher

https://doi.org/10.1021/acsanm.4c01970
ACS Appl. Nano Mater. XXXX, XXX, XXX−XXX

toxicity level in the same cellular models.[48] Nevertheless, these NPs showed a very low toxicity profile and favorable pharmacokinetics in vivo,[48] which promises similar negligible toxicity effects for laser-synthesized ZrN NPs.

The most important feature of laser-synthesized ZrN-based NPs comes from their particular plasmonic properties, which render possible a simultaneous manifestation of the photothermal effect along with near-field enhancement effects in the region of relative biological transparency (630−900 nm). As follows from our calculations shown in Figure 4a, the photoabsorption efficiency decreases with a red shift of the plasmonic feature, conditioned by the addition of oxide states into the NP composition. Nevertheless, for simulated core−shell geometries and optical constants, the absorption cross-sections σ_{abs} of relatively small ZrN NPs are still very high in the region of 650−720 nm and above, being only slightly inferior to relevant values for Au NPs of similar sizes near their resonance at 520 nm (see Figure 1a and data, e.g., from refs 4 and 58). Moreover, despite a slight blue shift of the extinction spectrum compared to TiN NP counterparts (670 nm compared to 700−720 nm), the efficiency of photoconversion of the engineered ZrN-based NPs is comparable to or even higher than the relevant values for TiN NPs reported in previous studies (see, e.g., ref 59). Our calculations also confirm that absorption σ_{abs} of 20 nm ZrN-based NPs with v_f = 0.15 of ZrO_2 in the NP core and a 3 nm oxide shell can be much higher in the spectral range of 650−750 nm than that of 20 nm TiN NPs having a similar oxide shell (Figure S13). Notice that a correct comparison of the absorption efficiencies of ZrN and TiN NPs is difficult for nanostructures prepared by different methods as these efficiencies strongly depend on the choice of NP architectures, ratio of elements in the composite matrix, and used optical constants. As an example, numerical simulations of nanocube structures composed of pure ZrN with typical sizes of about 100 nm demonstrated almost the same spectral shape and position of the plasmon resonance, as we observed in our calculations (Figure 1a).[60] This indicates that oxidation of the NP core is crucial to achieve a significant shift of the absorption band. The aggregation of particles (e.g., in the form of dimers) is another crucial factor, which can also be responsible for the spectral shift toward the NIR region.[61] The coupling between NPs leads to redistribution of the electric field and hence to modification of absorption and near-field enhancement properties. It is also important that the presence of high photothermal ability typically favors the implementation of efficient bioimaging modalities based on the photoacoustic response, which can be used in parallel with the photothermal therapy. As an example, we recently demonstrated that laser-synthesized TiN NPs can serve as efficient contrast agents in nonlinear photoacoustic imaging,[62] suggesting the possibility of using ZrN NPs in a similar way.

To demonstrate the therapeutic potential of laser-synthesized ZrN-based NPs, we assessed them in phototherapy tasks in a cellular model using 805 nm pumping radiation. The NPs were conjugated with the targeting molecule $Z_{HER1:1907}$ affibody, which is known to selectively recognize the HER1 receptor. HER1 overexpression has been identified in a wide range of human tumors, including nonsmall-cell lung cancer and small-cell carcinoma of the head and neck, thus presenting a clinically relevant target. The conjugation was done via carbodiimide chemistry to C-terms of the affibody, which are far from the recognizing center, to preserve the targeting ability of the molecule. As follows from flow cytometry analysis, the use of $Z_{HER1:1907}$ affibody conditioned the 119-fold targeting ability of NPs, which is an extremely high value for NPs since they always possess nonspecific binding to cells. Moreover, this value was similar to the specificity of full-size IgG, which is an evolutionally designed targeting protein, and was 3.4-fold higher than for previously reported HER1-targeted affibody-decorated Au-based NPs.[53] Photothermal biological evaluation performed on EGFR-positive cells showed their 100% death after only 5 min laser irradiation with moderate concentrations of ZrN NPs of about 100 μg mL^{-1} in the absence of any detectable effect on control cells without the HER1-receptor. This result is very impressive, illustrating the great potential of ZrN-based NPs for photothermal therapy. As one of the main advantages of ZrN NPs, the photothermal effect was obtained for relatively small sizes of NPs (20−30 nm), which are close to optimal sizes of nanomaterials for biomedical applications. For comparison, Au-based core−shells used in tasks of phototherapy have much larger sizes (typically larger than 100−150 nm)[12,13] to enable any therapeutic outcome in the region of biological transparency, while nanorods are normally stabilized by relatively toxic surfactants such as CTAB.[6,14]

Another advantage of the proposed NPs is the bioimaging option based on the ability of ZrN to locally enhance the electric field similarly to conventional plasmonic metals such as Au and Ag. As shown in Figure 4b, such an ability weakens under the red shift of the spectrum but still remains significant even with a high content of oxide states in the NP composition. To illustrate the imaging ability, we conjugated ZrN NPs with an Azo-based Raman reporter based on the Azo-CN-OH molecule and then managed to track the position of the ZrN NP-based conjugate in various compartments of HeLa cells (Figure 8). Despite a certain mismatch between the used wavelength (785 nm) and theoretically predicted maxima of field enhancement around 650−700 nm (Figure 4b), we clearly recorded the SERS effect on ZrN/ZrO_x NPs using Azo-CN-OH molecule as a Raman reporter (Figure S12). It should be noted that the assessment of near-field enhancement at this wavelength is very difficult due to the lack of optical constants in the literature and other factors such as possible aggregations of ZrN/ZrO_x NPs in biological experiments and a change in the refractive index of the environment due to the coating of NPs with Azo-CN-OH molecules, which are supposed to lead to a red shift of the absorption and near-field enhancement spectra. It should be noted that the near-field enhancement ability and related bioimaging option are hardly possible for TiN NPs as, in the case of this material, most absorbed energy is converted to heat.[20,21] We believe that the observed near-field enhancement ability of ZrN NPs can be useful for other applications, such as photocatalysis.

CONCLUSIONS

Using methods of fs laser ablation in liquid ambient, we synthesized relatively small (~20 nm) spherical ZrN-based NPs, which are capable of exhibiting broad plasmonic absorption bands with maxima around 660−670 and 610−630 nm for solutions prepared in acetone and ethanol, respectively, leading to prominent photothermal heating and near-field enhancement effects in the near-infrared window of relative biological transparency (630−900 nm). Our calculations show that such a plasmonic feature is highly red-shifted compared to pure ZrN NPs, which is explained by the inclusion of zirconium oxide ZrO_x ($1 < x < 2$) into the NPs' composition, as confirmed by structural analysis. The NPs

https://doi.org/10.1021/acsanm.4c01970
ACS Appl. Nano Mater. XXXX, XXX, XXX−XXX

demonstrated high safety in vitro, which was confirmed by results of MTT tests and flow cytometric analysis. To illustrate the targeted phototherapy effect, we show that after conjugation with the anti-HER1 affibody $Z_{HER1:1907}$, the NPs cause 100% cancer cell death under their illumination with an 805 nm pumping laser. Finally, profiting from a strong near-field enhancement of ZrN-based NPs, we demonstrated bioimaging functionality using a designed SERS probe based on the NP-conjugated Azo-CN-OH molecule as a Raman reporter. Laser-synthesized ZrN/ZrO_x NPs promise major advancements in theranostic modalities based on plasmonic nanomaterials.

MATERIALS AND METHODS

NP Synthesis. Zirconium nitride-based NPs were synthesized by femtosecond laser ablation of a hot-pressed ZrN (GoodFellow) target in acetone (Acros Organics, 99.5+%) or ethanol (Merck, 96%). The target was placed in a quartz cuvette filled with acetone or ethanol (50 mL) and fixed in a vertical position such that the distance between the inner wall of the cuvette and the surface of the target was 3 mm. A beam from a femtosecond Yb:KGW laser (Amplitude Systems, 1030 nm, 10 kHz, 490 fs for acetone; 50 kHz, 490 fs for ethanol) was attenuated to a value of 150 or 40 μJ per pulse for acetone and ethanol, respectively. The beam was deflected by reflective mirrors and focused by a plano-convex lens on the surface of the ZrN target. Finally, using the translation stage, the cuvette with the target was moved at a speed of 2.5 mm s^{-1}, and the ablation area was set to 5 mm × 5 mm.

Optical Characteristic Calculation. The absorption cross-section spectra were calculated using COMSOL Multiphysics software, radio frequency (RF) module, and frequency domain. The radius of the ZrN NP was set to 10.5 nm according to the experimentally observed log−normal distribution mode size: 10.5 nm core for ZrN; 7.5 nm core and 3 nm shell thickness for $ZrN@ZrO_2$ and $ZrN/ZrO_2@ZrO_2$ (v_f = 0.1 and 0.15). The Bruggeman effective medium approximation model was applied to estimate the refractive index (n,k) values of the ZrN/ZrO_2 mixed composition. Optical constants for Au, TiN, TiO_2, ZrN, ZrO_2, H_2O, and amorphous C were taken from corresponding sources.[63−70]

Characterization. NPs were characterized by a high-resolution transmission electron microscope (Jeol JEM-3010, 300 kV, 0.16 nm point-to-point in high-resolution mode) equipped with a GATAN Orius SC1000 (4k × 2.6k) camera. To prepare samples for TEM, ZrN NPs in acetone (10 μL) were dropped onto a carbon-coated copper grid (Oxford Instruments, 200 mesh) and dried under ambient conditions. The data for a distribution analysis and interplanar spacing values were obtained and calculated in Fiji ImageJ software.

XRD measurements of ZrN NP powder were performed in transmission mode. The instrument was equipped with a double reflection mirror (Osmic), an image plate detector (Mar345), and a high-brilliancy rotating anode (Rigaku RU-200BH, 50 kV, 50 mA). The radiation was Cu Kα (λ = 1.5418 Å), and the size of the beam was 0.5 × 0.5 mm^2. The maximum 2θ value was 65° (0.3° experimental resolution). The powder was obtained by drying a concentrated solution of ZrN NPs in acetone or ethanol on a silicon substrate under ambient conditions.

XPS measurements on ZrN-based NPs were carried out using a Thermo Scientific Nexsa G2 spectrometer with an operating pressure of ca. 1×10^{-9} Torr. Monochromatic Al Kα X-rays (1486.6 eV) with photoelectrons were collected from a 400 μm diameter analysis spot. Photoelectrons were collected at a 90° emission angle with a source-to-analyzer angle of 54.7°. A hemispherical analyzer determined electron kinetic energy using a pass energy of 200 eV for wide/survey scans and 50 eV for high-resolution scans. A flood gun was used for charge neutralization of nonconductive samples. The NP solution was deposited on a glass substrate and dried under ambient conditions prior to XPS measurements. Data on the atomic concentration of each component were extracted from XPS survey spectra using CasaXPS software (Shirley background correction).

Extinction spectra measurements were carried out using a UV−visible spectrophotometer equipped with an integrating sphere (UV-2600, Shimadzu) and a rectangular quartz cuvette (Fisherbrand, 10 mm optical path length).

A Thermo Scientific (Waltham, MA) DXR2 Raman confocal microscope was equipped with 633 nm−70 mW and 785 nm−30 mW laser modules and corresponding filter units. We used high-resolution blazing-angle (633 and 785 nm) gratings (50−1900 cm^{-1} spectral range) and an Olympus Plan N 100× (NA = 1.25) oil immersion objective to achieve single-cell imaging with high spatial resolution. We used Omnic software (Thermo Scientific, Waltham, MA) for imaging and image analysis. For cell imaging, the accumulation time was 2 × 300 ms and step −2 μm. The confocal pinhole was set at 50 μm. The average time of full image scanning was between 15 and 25 min.

The hydrodynamic diameter and ζ-potential were measured by dynamic light scattering and electrophoretic light scattering techniques, respectively, using a Malvern Zetasizer Nano ZS device (Malvern Instruments, UK). Hydrodynamic diameters describe mode values of number-weighted size distributions. The Smoluchowski approximation was used for ζ-potential calculation. To evaluate the colloidal stability of ZrN and ZrN@Chit NPs, we incubated them for 15 min in PBS (pH 7.4) and Dulbecco's modified Eagle's medium (DMEM) supplemented with 10% fetal bovine serum (FBS). Extinction spectra of ZrN and ZrN@Chit NPs were recorded using an Infinite M1000 PRO spectrophotometer (Tecan, Austria).

ZrN Chitosan Stabilization. Amino-terminated ZrN particles were obtained via electrostatic coating with chitosan oligosaccharide lactate by coincubation of ZrN (1 g L^{-1}) in water with chitosan oligosaccharide lactate (1 g L^{-1}, average Mw 5000) for 4 h at 80 °C with sequential washing from nonbound chitosan oligosaccharide lactate by triple centrifugation.

Study of Photothermal Properties. Photothermal heating of ZrN@Chit NPs was evaluated after irradiation of 1 mL of aqueous solution by an 808 nm laser source at 1.2 W power. The surrounding temperature was maintained at 23 °C during the irradiation and natural cooling. Samples were irradiated for 10 min to obtain heating kinetics for solutions of different concentrations and different laser powers, for a 5 min cyclic test.

Temperature measurements were performed using a FLIR C3-X thermal imaging camera (FLIR Systems, USA).

The photothermal conversion efficiency was determined using Roper's model of heat transfer

$$\eta(\%) = \frac{mC(\Delta T_{max}^{NP} - \Delta T_{max}^{water})}{\tau_c I(1 - 10^{-A_{808}})}$$

where m and C are mass and heat capacity of solvent (water), respectively; ΔT_{max}^{NP} and ΔT_{max}^{water} are elevations of temperature for NPs and water, respectively; τ_c is cooling temperature coefficient; I is irradiation power; A_{808} is the light absorbance of NP solution for 1 cm path length in water at λ = 808 nm. τ_c was determined from cooling kinetics $T(t)$ of solution as a slope of the negative logarithm of transfer driving force Θ versus time

$$\tau_c = \frac{-\ln(\Theta)}{t}$$

$$\Theta = \frac{T(t) - T^{amb}}{T_{max}^{NP} - T^{amb}}.$$

Affibody Conjugation to ZrN@Chit Particles. Covalent modification of ZrN NPs with affibody $Z_{HER1:1907}$ was carried out with the sodium salt of 1-ethyl-3-(3-dimethylamino propyl) carbodiimide (EDC, Sigma, Germany) and the sodium salt of *N*-hydroxysulfosuccinimide (sulfo-NHS, Sigma, Germany) as cross-linking agents via the formation of amide bonds between the carboxyl groups of the affibody and the ZrN@Chit amino groups. Affibody $Z_{HER1:1907}$ (50 μg) was activated with 50× molar excess of EDC in 0.1

https://doi.org/10.1021/acsanm.4c01970
ACS Appl. Nano Mater. XXXX, XXX, XXX−XXX

M 2-(*N*-morpholino) ethanesulfonic acid buffer (50 μL) for 40 min at 25 °C. Next, the activated protein was added to ZrN@Chit (500 μg) in borate buffer (0.4 M H_3BO_3, 70 mM $Na_2B_4O_7$, pH 8.0) and sonicated for several seconds. The reaction was carried out overnight at room temperature, followed by particle washing from nonbound protein by triple centrifugation at 5000*g* for 3 min.

Cell Culture. Human squamous carcinoma A431, human adenocarcinoma HeLa, and Chinese hamster ovary CHO cell lines were maintained in DMEM (HyClone, USA) supplemented with FBS (10%, HyClone, USA) and L-glutamine (2 mM, PanEko, Russia). The cells were incubated under a humidified atmosphere with CO_2 (5%) at 37 °C.

MTT Assay. For cytotoxicity evaluation, cells were seeded on a 96-well plate at 5×10^3 cells per well in DMEM (200 μL) supplemented with FBS (10%) and cultured for 48 h at different concentrations of ZrN@Chit NPs. Then, the medium was removed, and an MTT solution (100 μL, 0.5 g L^{-1} in DMEM) was added to the cells. Samples were incubated for 1 h at 37 °C. The MTT solution was then removed and DMSO (100 μL) was added to the wells; the plate was gently shaken until formazan crystals dissolved completely. The optical density of each well was measured using an Infinite 1000 PRO (Tecan, Austria) microplate reader at a wavelength of λ = 570 nm.

For photothermal treatment, cells were labeled with NPs, irradiated with an 805 nm laser, and seeded on a 96-well plate at 5×10^3 cells per well in DMEM (200 μL) supplemented with FBS (10%) and cultured for 48 h. After that, the MTT test was performed as described above.

Apoptosis Assay. To perform the analysis, 70−80% confluent cells were harvested using EDTA (2 mM), resuspended in a full culture medium, seeded at 24-well flat-bottomed culture plates, and incubated overnight under a humidified atmosphere containing CO_2 (5%) at 37 °C in DMEM. Then, NPs were added to get the final concentration of 50 or 200 μg mL^{-1} and incubated with cells for 48 h. After that, the cells were harvested with an EDTA solution (2 mM) in 1.5 mL tubes, centrifuged at 100 g for 5 min, and washed with cold PBS. For photothermal treatment, cells were irradiated by an 805 nm laser source for 5 min. Then, an Alexa Fluor 488 annexin V/Dead Cell apoptosis kit (Invitrogen, USA) with Alexa Fluor 488 annexin V and PI dyes was used for the analysis of apoptosis. Sample fluorescence was measured using a Novocyte 3000 VYB flow cytometer (ACEA Biosciences, USA). For the preparation of apoptotic cell-positive control, staurosporine (1 μM) was added to samples 4 h before the measurement. For the preparation of necrotic cell-positive control, heating of cells at 75 °C for 10 min was performed.

Flow Cytometry Analysis of Affibody Labeling. The cell suspension was incubated with FITC-modified affibody at a final concentration of 2 μg mL^{-1}, washed with PBS, and resuspended in PBS (300 μL) with BSA (1%) at a concentration of 10^6 cells mL^{-1}. Samples were analyzed in the FL1 channel (excitation laser—488 nm, emission filter—530/30 nm) using a BD Fortessa (BD, Holdrege, NE, USA) flow cytometer.

Flow Cytometry Analysis of NP Binding. The harvested cells were washed with PBS, resuspended in PBS (300 μL) with BSA (1%) at a concentration of 10^6 cells per mL, labeled for 20 min with NPs at a final concentration of 100 μg mL^{-1} of ZrN@Chit*$Z_{HER1:1907}$ or ZrN@Chit, washed from unbound particles with PBS, and analyzed using a Novocyte 3000 VYB flow cytometer in the side scatter channel (ACEA Biosciences, USA). Changes in cell populations' side scatter served as values characterizing the binding efficiency of NPs to cells.

Mass Spectrometry Analysis of NP Binding. The harvested cells were washed with PBS, resuspended in PBS (300 μL) with BSA (1%) at a concentration of 10^6 cells per mL, and labeled with NPs at a final concentration of 100, 200, and 400 μg mL^{-1} of ZrN@Chit*$Z_{HER1:1907}$. Then, after 20 min of coincubation, the cells were washed from unbound particles and resuspended in PBS. Then, the cells and NPs were dissolved with concentrated nitric acid under heating for 30 min at 80 °C, and Zr quantity was measured by inductively coupled mass spectrometry using a NexION 2000 device. ^{90}Zr was used for the analysis.

Clonogenic Assay. The clonogenic assay was performed as follows. 10^5 cells were labeled with NPs, irradiated by an 805 nm laser source, and then the cells were diluted 100 times with DMEM growth medium; 1000 cells were seeded for 1 well of 12-well flat-bottomed culture plates and cultured for 10 days. Next, the culture medium was decanted, and cells were washed with a PBS/methanol 50:50 mixture (500 μL), then fixed with methanol for 1 h at room temperature, and stained with 1% crystal violet for 15 min at room temperature. Next, cells were washed 10 times with water, followed by a visual evaluation of the grown cell colonies.

Cell Suspension Temperature Measurement. For temperature measurement during the irradiation, the cells were labeled with NPs as described above. Then, 3×10^5 cells with NPs were placed into a 1.5 mL tube and irradiated by an 808 nm laser source at 1200 mV. The temperature of the cell suspension with and without NPs was monitored with the FLIR MyOne (Teledyne FLIR, Santa Barbara, CA, USA) camera until the temperature reached a plateau. For repeated measurements, three independent samples were used for each NP concentration.

ZrN Modification for Raman Imaging. The surface modification of ZrN NPs was achieved by electrostatic coating with chitosan and intercalation of Azo-CN-OH. In brief, chitosan (300 μL, 3 mg mL^{-1} in deionized H_2O), 0.1 M sodium acetate buffer (300 μL, pH 4.4), and Azo (150 μL, 1 mg mL^{-1} in ethanol) were added to an aqueous ZrN NP suspension (2 mL). The mixture was stirred at room temperature for 10 min and subsequently centrifuged at 10,000 g for 15 min. The supernatant was discarded, and the resulting pellet was resuspended in distilled water (2 mL).

Raman Imaging. HeLa cells were grown in glass bottom dishes in advanced DMEM supplemented with 3% fetal calf serum (Thermo Fisher Scientific) and glutamax antibiotic−antimycotic solution (Thermo Fisher Scientific) at 37 °C in a humidified atmosphere containing CO_2 (5%). Before Raman imaging, the cells were incubated with surface-modified ZrN NPs (1 volume of NP stock solution per 10 volumes of DMEM) for 5 h. Following the incubation, cells were thoroughly washed in PBS and fixed for 15 min in PFA/PBS (3%). Then, Raman imaging was performed in fixed cells.

■ ASSOCIATED CONTENT

Supporting Information

The Supporting Information is available free of charge at https://pubs.acs.org/doi/10.1021/acsanm.4c01970.

Particle characterization, flow cytometry results, gating strategy, doxorubicin toxicity study by the MTT test, chromosomal DNA fragmentation evaluation, synergy quantification, clonogenic assay results, in vivo tumor model evaluation, and immunohistochemistry results (PDF)

■ AUTHOR INFORMATION

Corresponding Authors

Paras N. Prasad − *MEPhI, Institute of Engineering Physics for Biomedicine (PhysBio), Moscow 115409, Russia; The State University of New York, Buffalo, Department of Chemistry and Institute for Lasers, Photonics, and Biophotonics, University at Buffalo, New York, New York 14260, United States;* orcid.org/0000-0002-0905-7084; Email: pnprasad@buffalo.edu

Sergey M. Deyev − *Shemyakin-Ovchinnikov Institute of Bioorganic Chemistry of Russian Academy of Sciences, Moscow 117997, Russia; MEPhI, Institute of Engineering Physics for Biomedicine (PhysBio), Moscow 115409, Russia;* Email: biomem@mail.ru

Andrei V. Kabashin − *Aix-Marseille University, CNRS, LP3, Marseille 13288, France;* orcid.org/0000-0003-1549-7198; Email: andrei.kabashin@univ-amu.fr

https://doi.org/10.1021/acsanm.4c01970
ACS Appl. Nano Mater. XXXX, XXX, XXX−XXX

Authors

Andrei I. Pastukhov − *Aix-Marseille University, CNRS, LP3, Marseille 13288, France*

Victoria O. Shipunova − *Shemyakin-Ovchinnikov Institute of Bioorganic Chemistry of Russian Academy of Sciences, Moscow 117997, Russia*

Julia S. Babkova − *Shemyakin-Ovchinnikov Institute of Bioorganic Chemistry of Russian Academy of Sciences, Moscow 117997, Russia; MEPhI, Institute of Engineering Physics for Biomedicine (PhysBio), Moscow 115409, Russia*

Ivan V. Zelepukin − *Shemyakin-Ovchinnikov Institute of Bioorganic Chemistry of Russian Academy of Sciences, Moscow 117997, Russia; MEPhI, Institute of Engineering Physics for Biomedicine (PhysBio), Moscow 115409, Russia*

Micah Raab − *The State University of New York, Buffalo, Department of Chemistry and Institute for Lasers, Photonics, and Biophotonics, University at Buffalo, New York, New York 14260, United States*

Rebecca Schmitt − *The State University of New York, Buffalo, Department of Chemistry and Institute for Lasers, Photonics, and Biophotonics, University at Buffalo, New York, New York 14260, United States*

Ahmed Al-Kattan − *Aix-Marseille University, CNRS, LP3, Marseille 13288, France*

Artem Pliss − *The State University of New York, Buffalo, Department of Chemistry and Institute for Lasers, Photonics, and Biophotonics, University at Buffalo, New York, New York 14260, United States;* orcid.org/0000-0003-4867-4074

Andrey Kuzmin − *The State University of New York, Buffalo, Department of Chemistry and Institute for Lasers, Photonics, and Biophotonics, University at Buffalo, New York, New York 14260, United States;* orcid.org/0000-0001-7371-4643

Anton A. Popov − *MEPhI, Institute of Engineering Physics for Biomedicine (PhysBio), Moscow 115409, Russia*

Sergey M. Klimentov − *MEPhI, Institute of Engineering Physics for Biomedicine (PhysBio), Moscow 115409, Russia*

Complete contact information is available at: https://pubs.acs.org/10.1021/acsanm.4c01970

Author Contributions

The manuscript was written through the contributions of all authors. All authors have given approval to the final version of the manuscript.

Notes

The authors declare no competing financial interest.

■ ACKNOWLEDGMENTS

A.I.P. and A.V.K. acknowledge support from the French government under the France 2030 investment plan, as part of the Initiative d'Excellence d'Aix-Marseille Université—A*MIDEX" AMX-22-RE-AB-107 and the French National Research Agency (project ANR-23-CE07-0051). A.A.P. and S.M.K. acknowledge support from the Ministry of Science and Education of Russian Federation within the agreement no. 075-15-2021-1347. The work at the Institute for Lasers, Photonics and Biophotonics was supported by a fund from the office of Vice President for Research and Economic Development of the University at Buffalo. The authors would like to thank Damien Chaudanson and Alexandre Altié from CINAM, Aix-Marseille University, for their help in running TEM measurements and Vasile Heresanu from CINAM, Aix-Marseille University, for his help in running XRD measurements. The authors acknowledge the use of facilities and instrumentation supported by NSF through the Cornell University Materials Research Science and Engineering Center DMR-1719875.

■ REFERENCES

(1) Dreaden, E. C.; Alkilany, A. M.; Huang, X.; Murphy, C. J.; El-Sayed, M. A. The golden age: gold nanoparticles for biomedicine. *Chem. Soc. Rev.* **2012**, *41* (7), 2740−2779.

(2) Lim, W. Q.; Gao, Z. Plasmonic nanoparticles in biomedicine. *Nano Today* **2016**, *11* (2), 168−188.

(3) West, J. L.; Halas, N. J. Engineered Nanomaterials for Biophotonics Applications: Improving Sensing, Imaging, and Therapeutics. *Annu. Rev. Biomed. Eng.* **2003**, *5*, 285−292.

(4) Jain, P. K.; Lee, K. S.; El-Sayed, I. H.; El-Sayed, M. A. Calculated Absorption and Scattering Properties of Gold Nanoparticles of Different Size, Shape, and Composition: Applications in Biological Imaging and Biomedicine. *J. Phys. Chem. B* **2006**, *110* (14), 7238−7248.

(5) Zou, L.; Wang, H.; He, B.; Zeng, L.; Tan, T.; Cao, H.; He, X.; Zhang, Z.; Guo, S.; Li, Y. Current Approaches of Photothermal Therapy in Treating Cancer Metastasis with Nanotherapeutics. *Theranostics* **2016**, *6* (6), 762−772.

(6) Huang, X.; Jain, P. K.; El-Sayed, I. H.; El-Sayed, M. A. Plasmonic photothermal therapy (PPTT) using gold nanoparticles. *Lasers Med. Sci.* **2008**, *23* (3), 217−228.

(7) Lal, S.; Clare, S. E.; Halas, N. J. Nanoshell-Enabled Photothermal Cancer Therapy: Impending Clinical Impact. *Acc. Chem. Res.* **2008**, *41* (12), 1842−1851.

(8) Wang, Y.; Xie, X.; Wang, X.; Ku, G.; Gill, K. L.; O'Neal, D. P.; Stoica, G.; Wang, L. V. Photoacoustic Tomography of a Nanoshell Contrast Agent in the in Vivo Rat Brain. *Nano Lett.* **2004**, *4* (9), 1689−1692.

(9) Nie, S.; Emory, S. R. Probing Single Molecules and Single Nanoparticles by Surface-Enhanced Raman Scattering. *Science* **1997**, *275* (5303), 1102−1106.

(10) Kneipp, K.; Wang, Y.; Kneipp, H.; Perelman, L. T.; Itzkan, I.; Dasari, R. R.; Feld, M. S. Single Molecule Detection Using Surface-Enhanced Raman Scattering (SERS). *Phys. Rev. Lett.* **1997**, *78* (9), 1667−1670.

(11) Qian, X.; Peng, X.-H.; Ansari, D. O.; Yin-Goen, Q.; Chen, G. Z.; Shin, D. M.; Yang, L.; Young, A. N.; Wang, M. D.; Nie, S. In vivo tumor targeting and spectroscopic detection with surface-enhanced Raman nanoparticle tags. *Nat. Biotechnol.* **2008**, *26* (1), 83−90.

(12) Hirsch, L. R.; Stafford, R. J.; Bankson, J. A.; Sershen, S. R.; Rivera, B.; Price, R. E.; Hazle, J. D.; Halas, N. J.; West, J. L. Nanoshell-mediated near-infrared thermal therapy of tumors under magnetic resonance guidance. *Proc. Natl. Acad. Sci. U.S.A.* **2003**, *100* (23), 13549−13554.

(13) Loo, C.; Lowery, A.; Halas, N.; West, J.; Drezek, R. Immunotargeted Nanoshells for Integrated Cancer Imaging and Therapy. *Nano Lett.* **2005**, *5* (4), 709−711.

(14) Huang, X.; El-Sayed, I. H.; Qian, W.; El-Sayed, M. A. Cancer Cell Imaging and Photothermal Therapy in the Near-Infrared Region by Using Gold Nanorods. *J. Am. Chem. Soc.* **2006**, *128* (6), 2115−2120.

(15) Chen, J.; Wiley, B.; Li, Z.-Y.; Campbell, D.; Saeki, F.; Cang, H.; Au, L.; Lee, J.; Li, X.; Xia, Y. Gold Nanocages: Engineering Their Structure for Biomedical Applications. *Adv. Mater.* **2005**, *17* (18), 2255−2261.

(16) Liu, Y.; Mills, E. N.; Composto, R. J. Tuning optical properties of gold nanorods in polymer films through thermal reshaping. *J. Mater. Chem.* **2009**, *19* (18), 2704−2709.

(17) Petrova, H.; Perez Juste, J.; Pastoriza-Santos, I.; Hartland, G. V.; Liz-Marzán, L. M.; Mulvaney, P. On the temperature stability of gold nanorods: comparison between thermal and ultrafast laser-induced heating. *Phys. Chem. Chem. Phys.* **2006**, *8* (7), 814−821.

(18) Khlebtsov, N.; Dykman, L. Biodistribution and toxicity of engineered gold nanoparticles: a review of in vitro and in vivo studies. *Chem. Soc. Rev.* **2011**, *40* (3), 1647−1671.
(19) Naik, G. V.; Shalaev, V. M.; Boltasseva, A. Alternative Plasmonic Materials: Beyond Gold and Silver. *Adv. Mater.* **2013**, *25* (24), 3264−3294.
(20) Lalisse, A.; Tessier, G.; Plain, J.; Baffou, G. Plasmonic efficiencies of nanoparticles made of metal nitrides (TiN, ZrN) compared with gold. *Sci. Rep.* **2016**, *6* (1), 38647.
(21) Lalisse, A.; Tessier, G.; Plain, J.; Baffou, G. Quantifying the Efficiency of Plasmonic Materials for Near-Field Enhancement and Photothermal Conversion. *J. Phys. Chem. C* **2015**, *119* (45), 25518−25528.
(22) He, W.; Ai, K.; Jiang, C.; Li, Y.; Song, X.; Lu, L. Plasmonic titanium nitride nanoparticles for in vivo photoacoustic tomography imaging and photothermal cancer therapy. *Biomaterials* **2017**, *132*, 37−47.
(23) Popov, A. A.; Tselikov, G.; Dumas, N.; Berard, C.; Metwally, K.; Jones, N.; Al-Kattan, A.; Larrat, B.; Braguer, D.; Mensah, S.; Da Silva, A.; Estève, M. A.; Kabashin, A. V. Laser- synthesized TiN nanoparticles as promising plasmonic alternative for biomedical applications. *Sci. Rep.* **2019**, *9* (1), 1194.
(24) Exarhos, S.; Alvarez-Barragan, A.; Aytan, E.; Balandin, A. A.; Mangolini, L. Plasmonic Core-Shell Zirconium Nitride-Silicon Oxynitride Nanoparticles. *ACS Energy Lett.* **2018**, *3* (10), 2349−2356.
(25) Karaballi, R. A.; Humagain, G.; Fleischman, B. R. A.; Dasog, M. Synthesis of Plasmonic Group-4 Nitride Nanocrystals by Solid-State Metathesis. *Angew. Chem., Int. Ed.* **2019**, *58* (10), 3147−3150.
(26) Sugunakar Reddy, R.; Kamaraj, M.; Kamachi Mudali, U.; Chakravarthy, S. R.; Sarathi, R. Generation and characterization of zirconium nitride nanoparticles by wire explosion process. *Ceram. Int.* **2012**, *38* (7), 5507−5512.
(27) Kabashin, A. V.; Delaporte, P.; Pereira, A.; Grojo, D.; Torres, R.; Sarnet, T.; Sentis, M. Nanofabrication with Pulsed Lasers. *Nanoscale Res. Lett.* **2010**, *5* (3), 454−463.
(28) Zhang, D.; Gökce, B.; Barcikowski, S. Laser Synthesis and Processing of Colloids: Fundamentals and Applications. *Chem. Rev.* **2017**, *117* (5), 3990−4103.
(29) Kabashin, A. V.; Singh, A.; Swihart, M. T.; Zavestovskaya, I. N.; Prasad, P. N. Laser-Processed Nanosilicon: A Multifunctional Nanomaterial for Energy and Healthcare. *ACS Nano* **2019**, *13* (9), 9841−9867.
(30) Reinholdt, A.; Detemple, R.; Stepanov, A. L.; Weirich, T. E.; Kreibig, U. Novel nanoparticle matter: ZrN-nanoparticles. *Appl. Phys. B: Lasers Opt.* **2003**, *77* (6−7), 681−686.
(31) Fojtik, A.; Henglein, A. Laser ablation of films and suspended particles in a solvent - formation of cluster and colloid solutions. *Ber. Bunsen-Ges. Phys. Chem.* **1993**, *97* (2), 252−254.
(32) Kabashin, A. V.; Meunier, M. Synthesis of colloidal nanoparticles during femtosecond laser ablation of gold in water. *J. Appl. Phys.* **2003**, *94* (12), 7941−7943.
(33) Kabashin, A. V.; Meunier, M. Femtosecond laser ablation in aqueous solutions: a novel method to synthesize non-toxic metal colloids with controllable size. *J. Phys.: Conf. Ser.* **2007**, *59* (1), 354−359.
(34) Al-Kattan, A.; Ryabchikov, Y. V.; Baati, T.; Chirvony, V.; Sánchez-Royo, J. F.; Sentis, M.; Braguer, D.; Timoshenko, V. Y.; Estève, M. A.; Kabashin, A. V. Ultrapure laser-synthesized Si nanoparticles with variable oxidation states for biomedical applications. *J. Mater. Chem. B* **2016**, *4* (48), 7852−7858.
(35) Pastukhov, A. I.; Belyaev, I. B.; Bulmahn, J. C.; Zelepukin, I. V.; Popov, A. A.; Zavestovskaya, I. N.; Klimentov, S. M.; Deyev, S. M.; Prasad, P. N.; Kabashin, A. V. Laser-ablative aqueous synthesis and characterization of elemental boron nanoparticles for biomedical applications. *Sci. Rep.* **2022**, *12* (1), 9129.
(36) Riabov, A. B.; Yartys, V. A.; Hauback, B. C.; Guegan, P. W.; Wiesinger, G.; Harris, I. R. Hydrogenation behaviour, neutron diffraction studies and microstructural characterisation of boron oxide-doped Zr-V alloys. *J. Alloys Compd.* **1999**, *293*−*295*, 93−100.
(37) Nicholls, R. J.; Ni, N.; Lozano-Perez, S.; London, A.; McComb, D. W.; Nellist, P. D.; Grovenor, C. R. M.; Pickard, C. J.; Yates, J. R. Crystal Structure of the ZrO Phase at Zirconium/Zirconium Oxide Interfaces. *Adv. Eng. Mater.* **2015**, *17* (2), 211−215.
(38) Lackner, P.; Zou, Z.; Mayr, S.; Diebold, U.; Schmid, M. Using photoelectron spectroscopy to observe oxygen spillover to zirconia. *Phys. Chem. Chem. Phys.* **2019**, *21* (32), 17613−17620.
(39) Coloma Ribera, R.; van de Kruijs, R. W. E.; Sturm, J. M.; Yakshin, A. E.; Bijkerk, F. Intermixing and thermal oxidation of ZrO2 thin films grown on a-Si, SiN, and SiO2 by metallic and oxidic mode magnetron sputtering. *J. Appl. Phys.* **2017**, *121* (11), 115303.
(40) Pan, Y. First-principles investigation of structural stability, electronic and optical properties of suboxide (Zr3O). *Mater. Sci. Eng., B* **2022**, *281*, 115746.
(41) Dolgov, A.; Lopaev, D.; Lee, C. J.; Zoethout, E.; Medvedev, V.; Yakushev, O.; Bijkerk, F. Characterization of carbon contamination under ion and hot atom bombardment in a tin-plasma extreme ultraviolet light source. *Appl. Surf. Sci.* **2015**, *353*, 708−713.
(42) Hauser, D.; Auer, A.; Kunze-Liebhäuser, J.; Schwarz, S.; Bernardi, J.; Penner, S. Hybrid synthesis of zirconium oxycarbide nanopowders with defined and controlled composition. *RSC Adv.* **2019**, *9* (6), 3151−3156.
(43) Muneshwar, T.; Cadien, K. Comparing XPS on bare and capped ZrN films grown by plasma enhanced ALD: Effect of ambient oxidation. *Appl. Surf. Sci.* **2018**, *435*, 367−376.
(44) Visuttipitukul, P.; Leelaruedee, K.; Kuwahara, H.; Khamkongkaeo, A.; Yongvanich, N.; Chanlek, N.; Kidkhunthod, P.; Leelachao, S. Effect of zirconium addition on the phase evolution of chromium zirconium nitride prepared by magnetron sputtering. *Mater. Test.* **2020**, *62* (8), 783−787.
(45) Bharathiraja, S.; Bui, N. Q.; Manivasagan, P.; Moorthy, M. S.; Mondal, S.; Seo, H.; Phuoc, N. T.; Vy Phan, T. T.; Kim, H.; Lee, K. D.; Oh, J. Multimodal tumor-homing chitosan oligosaccharide-coated biocompatible palladium nanoparticles for photo-based imaging and therapy. *Sci. Rep.* **2018**, *8* (1), 500.
(46) Li, J.; Wang, S.; Fontana, F.; Tapeinos, C.; Shahbazi, M.-A.; Han, H.; Santos, H. A. Nanoparticles-based phototherapy systems for cancer treatment: Current status and clinical potential. *Bioact. Mater.* **2023**, *23*, 471−507.
(47) Li, J.; Zhang, W.; Ji, W.; Wang, J.; Wang, N.; Wu, W.; Wu, Q.; Hou, X.; Hu, W.; Li, L. Near infrared photothermal conversion materials: mechanism, preparation, and photothermal cancer therapy applications. *J. Mater. Chem. B* **2021**, *9* (38), 7909−7926.
(48) Zelepukin, I. V.; Popov, A. A.; Shipunova, V. O.; Tikhonowski, G. V.; Mirkasymov, A. B.; Popova-Kuznetsova, E. A.; Klimentov, S. M.; Kabashin, A. V.; Deyev, S. M. Laser-synthesized TiN nanoparticles for biomedical applications: Evaluation of safety, biodistribution and pharmacokinetics. *Mater. Sci. Eng., C* **2021**, *120*, 111717.
(49) Tang, Y.; Shen, Y.; Huang, L.; Lv, G.; Lei, C.; Fan, X.; Lin, F.; Zhang, Y.; Wu, L.; Yang, Y. In vitro cytotoxicity of gold nanorods in A549 cells. *Environ. Toxicol. Pharmacol.* **2015**, *39* (2), 871−878.
(50) Miao, Z.; Ren, G.; Liu, H.; Jiang, L.; Cheng, Z. Cy5.5-labeled Affibody molecule for near-infrared fluorescent optical imaging of epidermal growth factor receptor positive tumors. *J. Biomed. Opt.* **2010**, *15* (3), 036007.
(51) Rinkenauer, A. C.; Press, A. T.; Raasch, M.; Pietsch, C.; Schweizer, S.; Schwörer, S.; Rudolph, K. L.; Mosig, A.; Bauer, M.; Traeger, A.; Schubert, U. S. Comparison of the uptake of methacrylate-based nanoparticles in static and dynamic in vitro systems as well as in vivo. *J. Controlled Release* **2015**, *216*, 158−168.
(52) Zucker, R. M.; Daniel, K. M.; Massaro, E. J.; Karafas, S. J.; Degn, L. L.; Boyes, W. K. Detection of silver nanoparticles in cells by flow cytometry using light scatter and far-red fluorescence. *Cytometry, Part A* **2013**, *83* (10), 962−972.
(53) Jokerst, J. V.; Miao, Z.; Zavaleta, C.; Cheng, Z.; Gambhir, S. S. Affibody-Functionalized Gold-Silica Nanoparticles for Raman Molecular Imaging of the Epidermal Growth Factor Receptor. *Small* **2011**, *7* (5), 625−633.

https://doi.org/10.1021/acsanm.4c01970
ACS Appl. Nano Mater. XXXX, XXX, XXX−XXX

(54) Li, Y.; Heo, J.; Lim, C.-K.; Pliss, A.; Kachynski, A. V.; Kuzmin, A. N.; Kim, S.; Prasad, P. N. Organelle specific imaging in live cells and immuno-labeling using resonance Raman probe. *Biomaterials* **2015**, *53*, 25−31.
(55) Tselikov, G. I.; Ermolaev, G. A.; Popov, A. A.; Tikhonowski, G. V.; Panova, D. A.; Taradin, A. S.; Vyshnevyy, A. A.; Syuy, A. V.; Klimentov, S. M.; Novikov, S. M.; Evlyukhin, A. B.; Kabashin, A. V.; Arsenin, A. V.; Novoselov, K. S.; Volkov, V. S. Transition metal dichalcogenide nanospheres for high-refractive-index nanophotonics and biomedical theranostics. *Proc. Natl. Acad. Sci. U.S.A.* **2022**, *119* (39), No. e2208830119.
(56) Popov, A. A.; Swiatkowska-Warkocka, Z.; Marszalek, M.; Tselikov, G.; Zelepukin, I. V.; Al-Kattan, A.; Deyev, S. M.; Klimentov, S. M.; Itina, T. E.; Kabashin, A. V. Laser-Ablative Synthesis of Ultrapure Magneto-Plasmonic Core-Satellite Nanocomposites for Biomedical Applications. *Nanomaterials* **2022**, *12* (4), 649.
(57) Popov, A. A.; Tikhonowski, G. V.; Shakhov, P. V.; Popova-Kuznetsova, E. A.; Tselikov, G. I.; Romanov, R. I.; Markeev, A. M.; Klimentov, S. M.; Kabashin, A. V. Synthesis of Titanium Nitride Nanoparticles by Pulsed Laser Ablation in Different Aqueous and Organic Solutions. *Nanomaterials* **2022**, *12* (10), 1672.
(58) Loumaigne, M.; Midelet, C.; Doussineau, T.; Dugourd, P.; Antoine, R.; Stamboul, M.; Débarre, A.; Werts, M. H. V. Optical extinction and scattering cross sections of plasmonic nanoparticle dimers in aqueous suspension. *Nanoscale* **2016**, *8* (12), 6555−6570.
(59) Guler, U.; Suslov, S.; Kildishev, A. V.; Boltasseva, A.; Shalaev, V. M. Colloidal Plasmonic Titanium Nitride Nanoparticles: Properties and Applications. *Nanophotonics* **2015**, *4* (3), 269−276.
(60) Setoura, K.; Ito, S. Quantifying the durability of transition metal nitrides in thermoplasmonics at the single-nanoparticle level. *AIP Adv.* **2021**, *11* (11), 115027.
(61) Juneja, S.; Shishodia, M. S. Surface plasmon amplification in refractory transition metal nitrides based nanoparticle dimers. *Opt. Commun.* **2019**, *433*, 89−96.
(62) Das, A.; Pereira, A. C. M. V.; Popov, A. A.; Pastukhov, A.; Klimentov, S. M.; Kabashin, A. V.; Gomes, A. S. L. Plasmonically enhanced two-photon absorption induced photoacoustic microscopy with laser-synthesized TiN nanoparticles. *Appl. Phys. Lett.* **2022**, *121* (8), 083701.
(63) Olmon, R. L.; Slovick, B.; Johnson, T. W.; Shelton, D.; Oh, S.-H.; Boreman, G. D.; Raschke, M. B. Optical dielectric function of gold. *Phys. Rev. B* **2012**, *86* (23), 235147.
(64) Shkondin, E.; Repän, T.; Takayama, O.; Lavrinenko, A. V. High aspect ratio titanium nitride trench structures as plasmonic biosensor. *Opt. Mater. Express* **2017**, *7* (11), 4171−4182.
(65) DeVore, J. R. Refractive Indices of Rutile and Sphalerite. *J. Opt. Soc. Am.* **1951**, *41* (6), 416−419.
(66) Veszelei, M.; Andersson, K.; Ribbing, C. G.; Järrendahl, K.; Arwin, H. Optical constants and Drude analysis of sputtered zirconium nitride films. *Appl. Opt.* **1994**, *33* (10), 1993.
(67) Ribbing, C. G.; Roos, A. Zirconium Nitride (ZrN) Hafnium Nitride (HfN). In *Handbook of Optical Constants of Solids*; Palik, E. D., Ed.; Academic Press, 1997; pp 351−369.
(68) Wood, D. L.; Nassau, K. Refractive index of cubic zirconia stabilized with yttria. *Appl. Opt.* **1982**, *21* (16), 2978−2981.
(69) Hale, G. M.; Querry, M. R. Optical Constants of Water in the 200-nm to 200-μm Wavelength Region. *Appl. Opt.* **1973**, *12* (3), 555−563.
(70) Larruquert, J. I.; Rodríguez-de Marcos, L. V.; Méndez, J. A.; Martin, P. J.; Bendavid, A. High reflectance ta-C coatings in the extreme ultraviolet. *Opt. Express* **2013**, *21* (23), 27537−27549.

https://doi.org/10.1021/acsanm.4c01970
ACS Appl. Nano Mater. XXXX, XXX, XXX−XXX